

Elsevier Editorial System(tm) for Remote Sensing of Environment
Manuscript Draft

Manuscript Number:

Title: Characterization of Surface Directional Reflectance Properties over the US Southern Great Plains during the 2007 CLASIC Experiment

Article Type: Full length article

Keywords: Remote Sensing; Cloud Absorption Radiometer; BRDF; BRF; NDVI; EVI; Validation; Spatial Analysis; Geostatistics; Uncertainty Analysis; 6S; 2007 CLASIC Experiment; ARM Climate Research Facility; US Southern Great Plains; EOS Land Validation Core Sites

Corresponding Author: Dr. Miguel O. Román,

Corresponding Author's Institution: NASA Goddard Space Flight Center

First Author: Miguel O. Román

Order of Authors: Miguel O. Román; Charles K Gatebe; Crystal B Schaaf; Michael D King

Characterization of Surface Directional Reflectance Properties over the US Southern Great Plains during the 2007 CLASIC Experiment

Miguel O. Román ^{a,b*}, Charles K. Gatebe ^c,
Crystal B. Schaaf ^b, and Michael D. King ^d

^a *Terrestrial Information Systems Branch,*

NASA Goddard Space Flight Center, Greenbelt, Maryland, USA

^b *Dept. of Geography and Environment, Boston University, Boston, Massachusetts, USA*

^c *Goddard Earth Sciences and Technology Center, University of Maryland Baltimore County, Baltimore, Maryland , USA*

^d *Laboratory for Atmospheric and Space Physics, University of Colorado, Boulder, Colorado, USA*

* Corresponding author. Tel.: +1 301 614 5498; fax: +1 301 614 5269

E-mail address: Miguel.O.Roman@nasa.gov

Abstract

With the production of long-term Earth system data records from off-nadir multi-angle satellite measurements, the Bidirectional Reflectance Distribution Function (BRDF) is playing an increasingly important role. Because of the impact of surface reflectance anisotropy on global biophysical properties and climate variables, it is important to obtain an accurate representation of surface BRDFs. However, the spatial, temporal, and angular differences between satellite and *in-situ* measurements are subject to substantial uncertainties that are very difficult to quantify and are oftentimes ignored. The challenge of characterizing these uncertainties lies not only in the development of appropriate upscaling methods; but in the acquisition of an appropriate set of measurements for a given surface location, at a specific time, under the same illumination and viewing conditions, and at multiple spatial scales. In this study, we implemented a comprehensive uncertainty analysis suitable for such a task by analyzing high-quality, clear-sky, atmospherically-corrected surface directional reflectances acquired by NASA's airborne Cloud Absorption Radiometer (CAR). The experiment focused on four study plots representative of the most common surface conditions of the US Southern Great Plains during the 2007 Cloud and Land Surface Interaction Campaign (CLASIC). Angular distributions of the BRDF in the principal solar plane together with geostatistical analyses were used to examine the relationship between sensor spatial resolution and spatial autocorrelation across each study area. The techniques employed in this study will help to improve model parameterization of land surface reflectance by bridging the gap between small scale intensive field studies appropriate for modeling landscape patterns and distributions; and larger-scale and longer-term measurements appropriate for modeling the global climate system.

1. Introduction

The properties of anisotropically scattering surfaces in the reflection of solar incident light is described and specified by the bidirectional reflectance distribution function (BRDF) (Nicodemus 1977). The BRDF contains information relating to the physical structure and composition of land surface materials that cannot be inferred from their spectral properties alone (Barnsley et al. 1994). It is used in remote sensing applications for correction of view and illumination angle effects (Li et al. 1996; Strahler et al. 1996), for land cover classification schemes (Friedl and Strahler 2000), for cloud detection (d'Entremont et al. 1996; DiGirolamo and Davies 1994; Leroy et al. 1997), for atmospheric correction (Kaufman 1989), and other applications. The BRDF gives the lower radiometric boundary condition for any radiative transfer problem in the atmosphere; and is hence of relevance for climate modeling and energy budget investigations. The BRDF cannot be measured directly, but it can be estimated using models of surface scattering in conjunction with measurements of the Bidirectional Reflectance Factor (BRF), i.e., the ratio of the surface BRDF to that of a perfect Lambertian reflector under the same viewing and illumination conditions (Schaepman-Strub et al. 2006; Wenge and Xiaowen 2000).

In order for Earth System models to properly assimilate reflectance-based products, the uncertainty of angular reflectance retrievals must be quantified. However, accuracy assessment of satellite retrievals is a challenging task, due in part to the coarser spatial resolution of these products. At a scale of 250m+, it is difficult to relate satellite-derived reflectance to field or reference “ground truth” data (Cohen and Justice 1999). A number of upscaling approaches (Liang et al. 2002; Morisette et al. 2006; Privette et al. 1998) have combined field measurements and high resolution imagery (e.g., Landsat-ETM+ and EOS-ASTER) to produce retrievals that

are compatible with global datasets. However, the use of high-resolution products to derive information at a much coarser scale results in the lost of information in the “upscaled” representation due to image regularization (Jupp et al. 1988; 1989; Woodcock and Strahler 1987). Moreover, because of the lack of directional sampling, the use of single view-angle sensors as an intermediate between field BRF measurements and satellite retrievals results in additional uncertainties due to the intrinsic inconsistencies between nadir and off-nadir values.

In light of these challenges, only a few experiments have collected surface BRDFs from narrow instantaneous field-of-view (IFOV) radiometers. Airborne instruments, such as NASA’s Cloud Absorption Radiometer (CAR), have been used to assess MODerate Resolution Imaging Spectroradiometer (MODIS) and Multiangle Imaging SpectroRadiometer (MISR) retrievals (Abdou et al. 2006; Gatebe et al. 2003); while measurements from the airborne POLarization and Directionality of the Earth’s Reflectances (POLDER) instrument have been used to assess POLDER satellite retrievals (Leroy and Hautecoeur 1999). Ground-based sensors have been used to assess MODIS (Susaki et al. 2004) and MISR retrievals (Abdou et al. 2001). Ground-based PARABOLA (Portable Apparatus for Rapid Acquisition of Bidirectional Observations of Land and Atmosphere) measurements (Deering and Leone. 1986; Deering and Middleton. 1994) have the advantage of being able to control the angular sampling of the BRF (such as the principal solar plane) and are less influenced by atmospheric interference. The disadvantages of the PARABOLA data include low angular resolutions ($\sim 15^\circ$) and relatively smaller spatial footprints than satellite and airborne datasets. Conversely, aircraft measurements have higher angular resolutions and larger spatial coverage than PARABOLA data, making them more suitable for validation of satellite reflectance products. However, airborne sensors must also contend with issues such as aircraft stability, geolocation, gridding, and atmospheric correction.

In previous airborne experiments, surface BRDF retrievals have been compared against coincident ground and/or satellite measurements for validation purposes (Chen et al. 1997; Knobelspiesse et al. 2008; Leroy and Hautecoeur 1999). However, the intrinsic differences between such direct point-to-pixel comparisons are subject to substantial uncertainties. The empirical quality of BRDF data is rarely certain; but knowledge of these uncertainties is essential to understand their effect on higher-level surface biophysical properties (e.g., vegetation indices, surface albedo, LAI/FPAR, burned area, land cover, and land cover change). Estimation of these uncertainties would enable evaluation and partitioning of measurement and analytical (or model-driven) errors, which arise throughout the process of retrieving clear-sky observations to characterize surface reflectance properties. Previous studies have examined the scaling processes that give rise to these uncertainties; particularly in the relationships between vegetation indices (e.g., NDVI) and primary biophysical properties (e.g., LAI/FPAR) (Friedl et al. 1995; Rastetter et al. 1992). These assessments, however, have thus far been restricted to simulated environments that are largely simplified versions of reality. For more realistic retrieval scenarios, in which multiple underlying scales of variation are inherently present, the characterization of such measurement uncertainties becomes more challenging.

In this effort, we introduce a comprehensive uncertainty analysis that uses high-quality, clear-sky atmospherically-corrected surface directional reflectance acquired with NASA's Cloud Absorption Radiometer (CAR) (Gatebe et al. 2003; King et al. 1986). Linking instantaneous measurements from CAR for a given surface location and under the same conditions of illumination and viewing directions yields the underlying reflectance anisotropy (or BRDF shape) of that location. This information was used to quantify the differences in the BRDF measurements, and related measures of vegetation greenness, at multiple spatial scales.

The remainder of this paper is divided into three sections. Section 2 focuses on the definitions and major theory to be used, an overview of the CAR instrument, a description of the Southern Great Plains Central Facility (SGP-CF) and surrounding area, flight segment details, and ancillary datasets. Section 3 introduces the retrieval algorithm, data processing segment, and geostatistical approach. Results in Section 4 were partitioned into several spatial intervals and analyzed using a combination of spectral bands in addition to areal-mean and at-nadir indices of vegetation greenness. The semiempirical RossThick-LiSparseReciprocal (RTLSR) BRDF model (Lucht et al. 2000; Wanner et al. 1995; 1997) was then fitted to these retrieval scenarios to obtain a full BRDF model of the area. Finally, angular distributions of the BRDF in the principal solar plane together with geostatistical analyses were used to examine the relationship between sensor spatial resolution and spatial autocorrelation on the results obtained.

2. Background

2.1. RossThick-LiSparseReciprocal BRDF model

The airborne angular reflectance measurements acquired by the CAR instrument can be expanded into a linear sum of terms (or kernels) characterizing different scattering modes that, when combined, result in a kernel-based BRDF model (Roujean et al. 1992; Wanner et al. 1995). The superposition assumes that these modes are either spatially distinct within the scene viewed with little cross-coupling, physically distinct within a uniform canopy with negligible interaction, or empirically justified (Strahler et al. 1999). In this work, the kernel models employed in the MODIS (Collection V005) BRDF/albedo product were used. These parameters result from a reciprocal version of the semiempirical RossThick-LiSparseReciprocal BRDF model (RTLSR) (Lucht et al. 2000; Wanner et al. 1995; 1997):

$$BRDF(\theta_s, \theta_v, \Delta\phi, \lambda) \cong R(\theta_s, \theta_v, \Delta\phi, \Lambda)$$

$$= f_{iso}(\Lambda) + f_{vol}(\Lambda)K_{vol}(\theta_s, \theta_v, \Delta\phi) + f_{geo}(\Lambda)K_{geo}(\theta_s, \theta_v, \Delta\phi, P_4, P_5) \quad (1)$$

where:

$$K_{vol} = \frac{(\pi/2 - \xi) \cos \xi + \sin \xi}{\cos \theta_s + \cos \theta_v} - \frac{\pi}{4} \quad (2)$$

$$\cos \xi = \cos \theta_s \cos \theta_v + \sin \theta_s \sin \theta_v \cos \Delta\phi \quad (3)$$

$$K_{geo} = \frac{1 + \sec \theta'_s \sec \theta'_v + \tan \theta'_s \tan \theta'_v \cos \Delta\phi}{2} + \left[\frac{t - \sin t \cos t}{\pi} - 1 \right] (\sec \theta'_s + \sec \theta'_v) \quad (4)$$

$$\cos^2 t = \min \left\{ \left[\frac{P_4}{\sec \theta'_v + \sec \theta'_s} \right]^2 \left[D^2 + (\tan \theta'_v \tan \theta'_s \sin \Delta\phi)^2 \right], 1 \right\} \quad (5)$$

$$\tan \theta'_x = P_5 \tan \theta_x \quad ; \quad x = v \text{ or } s \quad (6)$$

$$D = \sqrt{\tan^2 \theta'_s \tan^2 \theta'_v - 2 \tan \theta'_s \tan \theta'_v \cos \Delta\phi} \quad (7)$$

In remote sensing measurement terms, the wavelength for the narrowband instruments of interest here is defined over the waveband Λ with limits $[\Lambda_{\min}, \Lambda_{\max}]$. Parameter $f_{iso}(\Lambda)$ is the isotropic scattering component and equivalent to a nadir-view ($\theta_v = 0$) nadir-sun ($\theta_s = 0$) reflectance retrieval. Parameter $f_{geo}(\Lambda)$ is the coefficient of the LiSparse-Reciprocal geometric scattering kernel K_{geo} , derived for a sparse ensemble of surfaces casting shadows on a Lambertian background (Li and Strahler 1992). Parameter $f_{vol}(\Lambda)$ is the coefficient for the RossThick volume scattering kernel K_{vol} , so called for its assumption of a dense leaf canopy (Ross 1981). $\Delta\phi$ is the relative solar azimuth angle ($\Delta\phi = \phi_s - \phi_v$) and ξ is the scattering phase angle between sun and view directions. The two constants, dimensionless crown relative height

($P_4 = h/b$) and shape ($P_5 = b/r$) parameters, have been fixed at $h/b = 2$ and $b/r = 1$ to invert the angular radiance data from MODIS. For these two parameters, h is the variable for height at which a crown center is located, b is the vertical half-axis of the modeled ellipsoid, and r is its horizontal radius.

2.2. *The Cloud Absorption Radiometer (CAR)*

A complete description of the CAR instrument is given by King et al. (1986) and updated by Gatebe et al. (2003) following an upgrade of the instrument in 2000. This brief overview, however, highlights some aspects of the instrument, as illustrated in Fig. 1; and summarizes the characteristics of the CAR instrument, platform, and scanning system as applicable during the 2007 Cloud and Land Surface Interaction Campaign (CLASIC).

The CAR is a 14-channel airborne scanning radiometer (with a spectral range from 0.34–2.3 μm) that can perform several functions including: (1) determining the single scattering albedo of clouds at selected wavelengths in the UV, visible, and near-infrared (King 1981; King et al. 1990); (2) acquiring imagery of clouds and the earth's surface; and (3) measuring the angular distribution of scattered radiation of various surfaces types (Gatebe et al. 2003).

The first eight channels of the CAR are continuously and simultaneously sampled, while the ninth registered channel is selected from among six channels on a filter wheel. For this study, the ninth channel (the filter wheel channels) was not used because of a problem with the detector. The CAR was designed to operate from a position mounted on an aircraft, either the tail or the nose or wing, so that a scan is unimpeded as it samples the sky and surface from zenith to nadir. The instantaneous-field-of-view of the radiometer is 1° (or ~ 17.5 mrad) and scans through a wide angle defined by an aperture of 190° and perpendicular to the plane's velocity vector. The instrument can be positioned to image any direction perpendicular to the flight track, but it is

mostly used to image the surface or sky from horizon to horizon or in the starboard from aircraft zenith to nadir, 95° on either side of the aircraft horizon. This permits observations of both zenith and nadir directions with as much as a 5° aircraft roll.

Fig. 2a. shows a typical flight pattern whereby the aircraft, with the CAR in the nose cone, flies a clockwise circular pattern above the surface repeatedly, drifting with the wind, scanning the underlying surface and much of the transmitted solar radiation from above, and making radiometric observations about every 1° in zenith angle. To measure the BRDF, multiple circular orbits over a particular surface can be acquired under clear sky conditions to smooth out small scale surface and atmospheric variations. These data are then averaged together to obtain a representative BRDF of the underlying surface within a ~ 3 km diameter defined by the flight circles.

During post processing, the CAR data are georectified and calibration coefficients are applied as described by Gatebe et al. (2005). The selected surface BRDF data are screened to achieve low noise level, a sufficient number of clear-sky retrievals, and roughly an even sampling of directional space. Using CAR in this way is therefore the most mobile and efficient way of measuring a representative surface BRDF; although it is still necessary to correct for atmospheric scattering effects both above and below the aircraft in order to isolate the reflectance properties of the underlying surface in the absence of an atmosphere.

2.3. *The Southern Great Plains Central Facility (SGP-CF)*

The heavily instrumented Southern Great Plains Central Facility (SGP-CF) (Fig. 2b - Fig. 2d) is located on 160 acres of cattle pasture and winter-wheat fields southeast of Lamont, Oklahoma. This station is situated at an elevation of 1014 m with temperatures averaging 34.7° C in the summer and -5.0° C in the winter. The climate is classified as sub-humid with an average

annual rainfall of 750 mm. During CAR Flight #1928 (24 June 2007), surface characteristics at the SGP-CF were typical for the rural Midwest of the United States in summer. The ground at the SGP-CF is relatively flat and covered by a patchwork of winter-wheat, corn fields, bare soil exposed by spring harvesting, and mixtures of pasture fields and trees. There are a few buildings and the occasional paved and dirt roads.

2.4. *Flight segment details*

There were a total of eleven CAR flights accomplished as part of the 2007 CLASIC experiment. However, only data from CLASIC Flight #1928 (the 10th flight out of Ponca City on 24 June 2007) was used in this study. A complete description of this and other CAR flights, including flight summaries (i.e., path, timing, and measurements), imagery, and mission details can be found at the CAR web site (WWW1). The 2007 CLASIC intense observing period (IOP) was affected by anomalous rainfall conditions that resulted in widespread and repeated flooding throughout the state of Oklahoma. Nevertheless, CLASIC Flight #1928 experienced favorable weather conditions and the flight executed a pattern that was optimal for BRDF measurements over the SGP-CF (Fig. 2a). During this flight, BRDF measurements were taken at several heights above ground level (i.e., 200 m, 600 m, 2000 m, and ~4000 m) under clear-sky conditions; with the exception of a small cluster of clouds, visually spotted far away from the station at $< 30^\circ$ from the southern horizon.

2.5. *Land cover characterization*

A number of intensive manual land cover surveys, vegetation measurements, and surface characterizations were conducted during CLASIC to obtain detailed vegetation land cover information. Several Advanced Wide Field Sensor (AWiFS) scenes, at 56 m spatial resolution,

were acquired to map the vegetation and land cover over the SGP domain, including the Central Facility. While there was little cloud-free imagery available for the actual CLASIC study period, a complex algorithm based upon a decision tree developed using previous studies (Doraiswamy et al. 2004; Friedl and Brodley 1997; Jackson et al. 2004), in combination with the available land survey data from April through September 2007, was used to create a land cover dataset with an overall accuracy of 82.66%.

Fig. 3 shows a 5 km \times 5 km subset of the CLASIC-AWiFS land cover dataset showing the areas that were sampled by the CAR instrument during Flight #1928. In order to improve the classification accuracy over each of these sections, a Quickbird scene acquired just 7 days after Flight #1928 (1 July 2007) was also used. Commission errors in the final classification were minimized by manually examining each of the study plots.

3. Methods

3.1. CAR data processing

The current CAR BRDF retrieval algorithm uses between ~76,400–114,600 directional measurements of radiance per channel per complete orbit to obtain a representative BRDF of the underlying surface as defined by a flight circle of ~3 km in diameter (Gatebe et al. 2003). These data are then averaged together to smooth out any small scale surface heterogeneities in the reflected solar radiation signal. Because of its ability to obtain BRDF measurements at several heights above ground level, the CAR can further provide independent estimates of surface BRDFs at multiple scales of resolution (~4.0–300 m – depending on view angle and altitude). Unlike most airborne radiometers, this instrument is actively stabilized by a sophisticated navigation system. Thus, each CAR scan is accompanied by high frequency navigation data that

allows for excellent geolocation of CAR image pixels. Accordingly, a new retrieval algorithm was developed to maximize the use of CAR observations for validation of satellite data and other terrestrial applications. The algorithm development process is summarized in Fig. 4 and detailed in Sections 3.1.1–3.1.4.

3.1.1. Radiometric calibration

Radiometric calibration of the CAR spectral channels was made at the NASA Goddard Space Flight Center Radiometric Calibration Facility (GSFC-RCF). A description of the calibration scheme, using a series of integrating spheres with diameters of 1.83, 1.22, and 0.51 m, covering all of the CAR’s spectral channels, can be found in (Gatebe et al. 2007). The conversion from CAR Digital Numbers (DNs) to Level 1 at sensor radiances is determined from the instrument’s response for at least two known radiance levels and then determining the instrument gain (slope) and offset (intercept) for each wavelength across the sensor band pass. The estimated errors associated with this radiometric conversion vary from $\pm 1\%$ to $\pm 3\%$ for all spectral channels (Gatebe et al. 2007; 2003). Radiometric calibration was performed prior to and after CLASIC. In the past, to determine a suitable calibration for a given flight during the experiment, a linear change between the preflight and postflight calibration was assumed as a function of only the number of flights flown during an entire campaign. For the CLASIC experiment, however, both the pre- and post-calibration coefficients were averaged. This routine made it simple to account for calibration uncertainties. Postflight/Preflight calibration ratios consequently varied between 0.9691 (at $\lambda = 0.472 \mu\text{m}$) and 1.1845 (at $\lambda = 0.340 \mu\text{m}$).

3.1.2. Geometric correction

The CAR navigation system provides the required parameters to perform geometric

correction of the acquired retrievals from each flight. At the beginning of each mirror scan cycle, the system records the current UTC time, altitude above the surface (h), aircraft heading, as well as the current solar zenith (θ_s) and solar azimuth (ϕ_s) angles. The instrument's viewing azimuthal angle (ϕ_v) is derived by adding 90° to the aircraft's heading. During Level 1 processing, the actual pixel-viewing zenith angle (or scan angle) (θ_u) is determined for each of the ~ 382 pixels obtained across each scan line. Since the CAR instrument's scan begins at zenith, we subtract 180° to obtain a nadir-looking angle equal to 0° : $\theta_v = 180 - \theta_u$. Given the above parameters, and the geographical coordinates of the nadir pixel, $[lat_{nadir}, lon_{nadir}]$, the coordinates of the other off-nadir pixels along the scan line (i.e., from horizon to near-nadir), $[lat_{off-nadir}, lon_{off-nadir}]$, can be derived using the following equations:

$$lat_{off-nadir}^\circ = \sin^{-1} \left[\sin(lat_{nadir}) \cdot \cos \left[\frac{d}{R_\oplus} \right] + \cos(lat_{nadir}) \cdot \sin \left[\frac{d}{R_\oplus} \right] \cdot \cos(\phi_v) \right] \quad (8)$$

$$lon_{off-nadir}^\circ = - \left(a - 360^\circ \cdot \left\lfloor \frac{a}{360^\circ} \right\rfloor \right) + 180^\circ \quad (9)$$

where:

$$d = h \tan(\theta_v) \quad (10)$$

$$a = lon_{nadir} - dlon + 180^\circ \quad (11)$$

$$dlon = \begin{cases} 0 & \cos(lat_{nadir}) = 0 \\ \psi & \cos(lat_{nadir}) \neq 0 \end{cases} \quad (12)$$

$$\begin{aligned}
260 \quad \psi = & \begin{cases} \arctan\left(\frac{y}{x}\right) & x > 0 \\ \pi + \arctan\left(\frac{y}{x}\right) & y \geq 0, x < 0 \\ -\pi + \arctan\left(\frac{y}{x}\right) & y < 0, x < 0 \\ \frac{\pi}{2} & y > 0, x = 0 \\ -\frac{\pi}{2} & y < 0, x = 0 \\ undefined & y = 0, x = 0 \end{cases} \quad (13)
\end{aligned}$$

$$\begin{aligned}
261 \quad x = & \cos\left[\frac{d}{R_{\otimes}}\right] - \sin(lat_{nadir}) \cdot \sin(lat_{off-nadir}) \quad (14)
\end{aligned}$$

$$\begin{aligned}
262 \quad y = & \sin(\phi_v) \cdot \sin\left[\frac{d}{R_{\otimes}}\right] \cdot \cos(lat_{nadir}) \quad (15)
\end{aligned}$$

263 d [km] is the distance from the CAR instrument to the off-nadir pixel and R_{\otimes} is the earth's radius
264 $\approx 6,378.13$ km. Assuming a circular flight path, a small bank angle and an aircraft speed of ~ 150
265 ms^{-1} , the CAR can make radiometric observations about every 1° in azimuth and about 1° in
266 zenith angle. Thus, the image pixel width directly increases as a function of pixel-viewing zenith
267 angle (θ_v). The size of a nadir-looking CAR pixel (P_{nadir}) is a function of the altitude above
268 ground level (h) as well as the instrument field-of-view ($\alpha = 1^\circ \approx 17.45$ mrad):

$$\begin{aligned}
269 \quad P_{nadir} = & \alpha \cdot h \quad (16)
\end{aligned}$$

270 Off-nadir pixel widths (P_θ) are then calculated based on the relationship:

$$\begin{aligned}
271 \quad P_\theta = & P_{nadir} \cdot \sec^2 \theta_v \quad (17)
\end{aligned}$$

272

273

3.1.3. Atmospheric correction

The effects due to atmospheric scattering and absorption by aerosols and gases in the atmosphere were removed using the 6SV4.1 radiative transfer code (Kotchenova et al. 2006). The 6SV model allows us to determine the attenuation of solar irradiance under clear-sky conditions at the surface. The code is based on the method of successive orders of scattering approximations and its current vector version is also capable of accounting for radiation polarization. Aerosol optical properties were retrieved from CAR measurements in combination with AERONET measurements as described in Gatebe et al. (2009) for CLASIC Flight #1928. These inversions produced an estimate of the complex refractive index $n(\lambda) = 1.3606 - 0.021i$ as well as aerosol column particle size parameters at 22 size bins (Fig. 4c). The total column water vapor $q = 1.42 \text{ g cm}^{-2}$ (0.62 g cm^{-2} above the aircraft) was also obtained from ground-based sun photometer measurements, and an O_3 column amount was assumed to be 344 m atm-cm . The aerosol optical thickness $\tau_{0.55\mu\text{m}} = 0.1638$ (0.1405 above the aircraft when flying at $\sim 200 \text{ m}$ above the surface). These results were acquired using Level 2 aerosol optical thickness data from an AERONET sunphotometer (Holben et al. 2001) that is based at the SGP-CF site. The 6SV computation was performed assuming a homogenous surface with a Lambertian reflectance, and solar zenith angle range of $48.1^\circ - 74.0^\circ$ (depending on flight time).

3.1.3. RossThick-LiSparseReciprocal BRDF model inversions

The RTLSR BRDF kernel model parameters were obtained by iterating between the BRF data available for a given surface location and the RossThick volume scattering (K_{vol}) and LiSparse-Reciprocal geometric scattering (K_{geo}) kernel values, until the modeled calculated reflectance $R(\theta_v)$ matched the observed retrievals $\rho(\theta_v)$ (Strahler et al. 1999). The kernel fit to the BRF data uses a least square estimate of the kernel coefficients. Thus, a vector of kernel

297 coefficients, f_k , can be expressed by using a simple matrix inversion:

$$298 \quad R(\theta_v) = \left(\left[K_x(\theta_v) K_x(\theta_v) \right]^1 K_x(\theta_v) \right) \rho(\theta_v) \quad (18)$$

$$= \sum f_k K_x(\theta_v)$$

$$299 \quad e^2 = \frac{\sum (\rho(\theta_v) - R(\theta_v))^2}{n} \quad (19)$$

300 where $\rho(\theta_v)$ is a $1 \times n$ matrix, representing the column vector of n measured BRF values and K is
 301 an $m \times n$ matrix, representing the column vectors of the m kernels values for each of the n
 302 measurement geometries. The iteration was repeated a number of times for each CAR spectral
 303 band until e^2 reached a constant minima. Note that K , f_k , R , and ρ depend on the same set of
 304 wavelength (Λ) and geometric parameters (θ_s , $\Delta\phi$), so those subscripts have been omitted from
 305 the above equations.

306 3.2. Geostatistical approach

307 One of the most efficiently used geostatistical tools for describing the spatial characteristics
 308 of remotely-sensed data products is the variogram (Carroll and Cressie 1996; Davis 1986; Isaaks
 309 and Srivastava 1989; Matern 1963). Variogram analysis consists of the experimental (semi-)
 310 variogram, $\gamma_E(h)$, which is a function that relates semivariance (or dissimilarity) of data points to
 311 the distance that separates them. It is mathematically defined as half of the average squared
 312 difference between two variables at two locations:

$$313 \quad \gamma_E(h) = 0.5 \frac{\sum_{i=1}^{N(h)} (z_{xi} - z_{xi+h})^2}{N(h)} \quad (20)$$

314 where: z_x is a measurement at location x ; and z_{x+h} is a measurement at another location within a
 315 lag distance h . The coefficients of the isotropic spherical variogram model (Materon 1963),
 316 namely the range (a), sill (c), and nugget variance (c_0), can then be optimized to fit the
 317 experimental semivariogram:

$$318 \quad \gamma_{sph}(h) = \begin{cases} c_0 + c \left[1.5 \frac{h}{a} - 0.5 \frac{h^3}{a^3} \right] & \text{for } 0 \leq h \leq a \\ c_0 + c & \text{for } h > a \end{cases} \quad (21)$$

319 The square root of the nugget variance has been used to estimate the ratio of signal to random
 320 variability or “noise”, i.e., a form of measurement error that includes both random sensor noise
 321 and intrapixel variability (i.e., variability within a pixel) (Carr and Myers 1984; Curran and
 322 Dungan 1989). Of particular interest in this study is the proportion of structural variation (Li and
 323 Reynolds 1995):

$$324 \quad SH = \frac{c - c_0}{c} \quad (22)$$

325 SH is a measure that describes the amount of landscape variability that is attributable to spatial
 326 (as opposed to random) effects. This measure can be obtained by subtracting the variogram
 327 nugget (c_0) from the sill (c) and then dividing by the sill. Since the sill represents the maximum
 328 (overall) variation, and the nugget represents pure random variation, subtracting both terms
 329 results in a measure of spatially-correlated variation.

330 Previous studies have extracted variogram model coefficients from Landsat ETM+ data to
 331 characterize the variability of point (tower) measurements of surface albedo relative to a much
 332 larger ($>1.0\text{km}$) pixel area (Román et al. 2009; 2010; Susaki et al. 2007). The objective then was

to understand albedo retrieval uncertainties both in terms of the representativeness of the field data and its relationship to the larger satellite pixel. What's interesting about the BRF retrievals obtained by the CAR instrument is that they allow us to further characterize the effects of measured underlying variation within the footprint of satellite sensor retrievals. Thus, the more one knows about the underlying variation, the more accurately one should be able to estimate measurement errors (Atkinson 1997).

4. Results and Discussion

Figs. 5-8 show the spatial distribution of surface BRF measurements acquired by the CAR instrument during CLASIC Flight #1928. The study plots were located on a pasture field $\sim 650 \text{ m}^2$ (Fig. 5); a corn field $\sim 350 \text{ m}^2$ (Fig. 6); a senescent winter-wheat field $\sim 785 \text{ m}^2$ (Fig. 7); and a stubble field $\sim 565 \text{ m}^2$ (Fig. 8). The BRF retrievals have been partitioned into various spatial intervals (from $5.0\text{-}250 \text{ m}^2$) showing both their size and location (red circles); and have been superimposed against a QuickBird scene acquired just 7 days after CLASIC Flight #1928 (1 July 2007). Aside from the presence of clouds (Fig. 5a) and cloud shadows (Fig. 7a), the surface conditions remained largely unchanged throughout this period. Thus, this acquisition should be a fairly accurate representation of the actual field conditions throughout the experiment.

Each study plot is characterized by varying degrees of landscape variability; with stubble identified as the most homogeneous plot and winter-wheat as the least. It is interesting to notice how small scale variations across each of the study plots (e.g., patches of bare soil in Fig. 5 or tailwater ditches in Fig. 6) are being captured by the different spatial intervals. Despite their small size relative to the dominant landscape, these patches have significantly different BRDF signatures and will consequently introduce some errors in the BRDF retrievals.

Figs. 5-8 also include a set of polar plots illustrating the angular distribution of the BRF measurements. The viewing zenith angle is represented as the radial distance from the center and the relative (view-solar) azimuth angle as the length of the arc on the respective zenith circle. The principal plane resides in the vertical plane through the center of the plot. In general, BRF measurements with pixel sizes < 40 m were sampled within a scan angle range of $25^{\circ} \pm 15^{\circ}$; while BRF retrievals > 40 m were sampled at a range of $45^{\circ} \pm 10^{\circ}$. These measurements are thus equivalent to a synchronized retrieval from a near-nadir high-spatial resolution sensor (e.g., Landsat-ETM+ and ASTER) and an off-nadir multi-angle moderate resolution sensor (e.g., MODIS, MISR, or POLDER).

It is useful to characterize the measurement uncertainties directly on the reflectance-based products themselves, as the errors are not spatially and/or spectrally independent. In particular, vegetation indices (VIs) such as the Normalized Difference Vegetation Index (NDVI) (Tucker 1979) and the Enhanced Vegetation Index (EVI) (Huete et al. 1994) are calculated from surface BRFs and are often used to monitor the Earth's terrestrial photosynthetic vegetation activity. BRDF model information can also be used to correct directional reflectance to a standard viewing and illumination geometry. Accordingly, Nadir BRDF-Adjusted Reflectances (NBAR) obtained from RTLSR-BRDF model inversions (Schaaf et al. 2002) are oftentimes used in applications where more stable and consistent reflectance-driven vegetation signatures (e.g., NDVI and EVI) are favored to composited values (Zhang et al. 2009). As such, it is important to distinguish the differences between:

1. NBAR-based VIs, which are derived from RTLSR-BRDF model reflectance corrected to both a common viewing ($\theta_v = 0^{\circ}$) and illumination ($\theta_s = \text{Local Solar Noon (LSN)}$) geometry.

2. Nadir VIs that are based on BRF measurements obtained by the CAR instrument at nadir ($\theta_v = 0^\circ$) under different illumination conditions.

3. Areal-mean VIs, which are based on BRF measurements obtained by the CAR instrument over a full range of viewing and illumination conditions.

The impacts of the measurement uncertainties associated with these reflectance-based products will primarily depend on: (1) the number of samples obtained for a particular spatial threshold; (2) the quality of each observation; and (3) the degree to which directional effects are minimized.

Tables 1 to 4 provide summary statistics for each study plot using the same BRF measurements as Figs. 5-8. For each spatial interval, the sample size, mean scan angle, and mean pixel size are shown alongside the various data products of interest. These include:

1. Areal-mean estimates of surface BRF (cf. Direct method) compared against NBAR retrievals (cf. RTLSR Model: NBAR) for CAR bands #3 (0.472 μm), #4 (0.682 μm), and #5 (0.870 μm).
2. At-nadir retrievals of NDVI and EVI compared against NBAR retrievals.
3. Areal-mean estimates of NDVI and EVI compared against NBAR retrievals.

It is important to distinguish the difference between the different sets of summary statistics presented in Tables 1 to 4. For instance, the RTLSR model uncertainty (eq. 22) describes the deviation of the RTLSR model-fits from clear-sky observations and is a band dependent function weighted by observation quality (Shuai et al. 2008). Conversely, the measurement uncertainty describes the deviation of CAR retrievals (x_i) at all spatial intervals (n) from its weighted mean (\bar{x}):

$$Abs.RMSE = \sqrt{\frac{1}{n} \sum_{i=1}^n (x_i - \bar{x})^2} \quad (23)$$

400 where:

$$401 \quad \bar{x} = \frac{\sum_{i=1}^n (w_i \cdot x_i)}{\sum_{i=1}^n w_i} \quad (24)$$

$$402 \quad \text{Rel.RMSE} = \frac{\text{Abs.RMSE}}{\bar{x}} \% \quad (25)$$

403 The weights (w_i) are determined by the sample size of each spatial interval. These statistics,
404 therefore, provide a benchmark for evaluating the consistency of CAR retrievals at multiple
405 scales of resolution.

406 Measurement uncertainties are reported both before and after corrections for BRDF
407 effects and normalizations to standard viewing/solar geometries have been applied. Results show
408 how these corrections reduce the variability in the areal-mean BRF measurements by an average
409 of 9.18%, 4.13%, and 6.25% for CAR Bands #3, #4, and #5; and by an average of 6.63% and
410 7.80% for NDVI and EVI (respectively). The at-nadir retrievals of NDVI and EVI (cf. direct
411 method) were also consistently lower than the areal-mean estimates by an average of 5.75% and
412 2.95%; and the additional correction to a standard solar geometry (at LSN) further reduces the
413 uncertainty by an additional 0.89% and 4.85% (respectively).

414 The measurement uncertainty, after correction for BRDF effects, remains within relative
415 bounds of 11.04%, 14.37%, 12.72% for CAR bands #3, #4, and #5; and 5.26% and 10.24% for
416 NDVI and EVI (respectively). Other possible causes of uncertainty, e.g., those related to the
417 calibration, geolocation, and atmospheric correction stages, have been addressed in Section #3;
418 and a number of quality assurance routines (e.g., pre- and post-calibration coefficient monitoring
419 and removal of CAR observations at $\text{SZA} > 75^\circ$) have been implemented to reduce them. Thus, it

is reasonable to conclude that the remaining uncertainties are driven by the underlying sources of spatial variation both within the spatial footprint of each study plot and each spatial interval. These variations are also linked to undersampling effects. Notice that some spatial intervals (particularly 80-100m) have large sampling gaps that cover a narrow portion of the BRDF hemisphere. To minimize the effects due to undersampling, only the higher-quality spatial intervals, i.e. with complete spatial coverages and broader angular distributions ($> \pm 10^\circ$), were used.

Figs. 9 and 10 illustrate the angular distribution of CAR bands #3, #4, and #5 (Fig. 9) as well as NDVI and EVI (Fig. 10) in the principal solar plane. These plots were examined under three different illumination conditions (at $\text{SZA} = 15^\circ$ (~LSN), 30° , and 60°). Results were derived from RTLSR-BRDF model inversions taken over each of the study plots at both low (100-250 m) and high spatial resolutions; the latter being selected based on the spatial interval < 60 m of with the highest quality and sampling efficiency. This analysis is thus equivalent to comparing model retrievals from a sensor that produces near-nadir Lambertian BRDFs against model retrievals from a sensor that produces off-nadir/multi-angle views at a coarser spatial resolution. Results show how the shape of the BRDF tends to diverge between the two spatial intervals as we move away from nadir and as the SZA increases. For the VIs in Fig. 10, the spatial variation was very site-dependent, with Plot #1 and Plot #3 (Figs. 10a and 10c, respectively) remaining almost constant at both spatial intervals (for $\text{SZA} < 60^\circ$). Conversely, the VIs on Plot #2 and Plot #4 (Figs. 10b and 10d, respectively) varied significantly as a function of SZA; with the movement of the hotspot region affecting both the shape and magnitude of the VIs.

The percentage difference (at $\theta_v = 0^\circ$ and $\theta_s = \text{LSN}$) between the modeled retrievals at both low and high spatial resolution resulted in relative bounds of 12.25%, 11.87%, 11.74% for Bands #3, #4, and #5; and 7.36% and 13.57% for NDVI and EVI (respectively). These results are consistent with the summary statistics in Tables 1-4.

The experimental variograms in Figs. 11-14 show the variation in CAR retrievals as a function of spatial intervals and separation distance. The geostatistical analysis includes BRFs (i.e., CAR bands #3, #4, and #5) as well as vegetation indices (i.e., NDVI and EVI). The distance between lags was defined at 5.0 m, which reasonably matches a CAR nadir pixel at the lowest flight altitude (~200 m). Notice that variograms that exhibit no spatial dependence remain constant at increased lag distances. This is the case for CAR bands #3 and #4, which exhibited random patterns of variation. Another interesting feature is that the variograms at the larger spatial intervals (particularly for CAR pixels > 100 m) also have higher semivariance. This runs contradictory to the effect of image regularization on the experimental variogram (Jupp et al. 1988; 1989; Woodcock and Strahler 1987); which predicts lower semivariance at moderate spatial resolutions. It is therefore important to understand the differences between the spatial patterns observed when increasing the size of the units of regularization, which is analogous to coarsening the spatial resolution (Woodcock et al. 1988); and the spatial patterns that result from interactions between CAR observations at spatial intervals that are independent of each other. Unlike the former, the residual variation of CAR retrievals is influenced by two major sampling factors: First, the mean scan angle generally increases with spatial interval (see Tables 1-4). As a result, the larger CAR pixels have a tendency to be sampled near the extreme regions of the BRDF hemisphere (i.e., the hot-spot and dark-spot). Second, the spread of the variability between pixel sizes (as measured by the standard deviation from the mean pixel size) increases

from one spatial interval to the other. Under these sampling conditions, if the landscape is represented by a single (homogeneous) ecosystem type, then variograms taken at increasingly smaller spatial intervals should have consistently lower within-pixel-variance and, accordingly, lower semivariance. Such is the case with the stubble plot in Fig. 8. With the exception of the 80–100 m threshold (which suffered from undersampling bias), the spatial intervals in Fig. 14 show a consistent increase in semivariance. However, as landscape heterogeneity increases, multiple underlying scales of variation begin to undercut this trend. For instance, the semivariance for CAR band #5 in Fig. 13c (winter-wheat) is higher at smaller spatial intervals (< 20 m) and is further influenced by localized conditions at distances < 30 m. This trend can be attributed to a small patch of grassland that is crossing straight through the center of the winter-wheat field and is roughly 5-30 m thick (see Fig.7a) The fact that semivariance at spatial scales < 20 m can be as high as the semivariance at scales > 60 m underscores the importance of characterizing BRDF retrieval uncertainties introduced by intrapixel variations and spatially independent noise. This also applies to vegetation indices; which are dependent on multiple spectral signatures that have their own residual sources of variation.

Fig. 15 shows the proportion of structural variation (SH) as a function of spatial intervals for CAR band #3, #4, #5, NDVI, and EVI. The plots show how the influence of random sensor noise and intrapixel variability varies between spatial thresholds. For instance, the undersampling conditions at the 80-100 m spatial intervals resulted in slightly lower values for SH ; particularly for the pasture and corn fields (Fig. 15a and 15b, respectively). In general, however, the results confirm that systematic and random variations in CAR reflectance data are considerably small over the range of surface conditions that were tested.

5. Summary

In previous experiments using airborne angular reflectance measurements, it is common to acquire instantaneous retrievals of surface BRDFs, and then compare them directly against coincident ground and/or satellite measurements for validation purposes. As we note, these “point-to-pixel” comparisons are influenced by multiple underlying sources of variation that introduce measurement uncertainties within the footprint of satellite sensor retrievals. In this effort, we characterized the major sources of such uncertainties by analyzing high-quality, clear-sky, atmospherically-corrected surface directional reflectances (or BRFs) acquired by NASA’s airborne Cloud Absorption Radiometer (CAR).

During CLASIC Flight #1928, BRDF measurements were taken at several heights above ground level (i.e., 200 m, 600 m, 2000 m, and ~4000 m) under clear-sky conditions. Using CAR in this way provides a unique retrieval scenario equivalent to a synchronized acquisition from both a near-nadir high-spatial resolution sensor (e.g., Landsat-ETM+ and ASTER) and an off-nadir multi-angle moderate resolution sensor (e.g., MODIS, MISR, or POLDER).

Analyses of areal-mean and at-nadir indices of vegetation greenness over four study plots demonstrate how BRDF normalization of surface directional reflectance improves the consistency of the BRF retrievals (using multiple spatial intervals from 5.0-250 m²) by an average of 9.18%, 4.13%, and 6.25% for CAR Bands #3, #4, and #5; and by an average of 6.63% and 7.80% for NDVI and EVI (respectively).

Angular distributions of the BRDF in the principal solar plane together with geostatistical analyses were used to: (1) characterize the residual sources of underlying spatial variation; (2) identify the scale(s) at which the greatest significant variation occurs; and (3) understand the physical processes that influence landscape patterns and distributions. The variability between

CAR BRF retrievals increases from one spatial interval to the other (mainly as a function of pixel size and view angle). However, as landscape heterogeneity increases, multiple underlying scales of variation will undercut this trend and introduce residual spatial patterns that are intrinsic to a specific location. These uncertainties were characterized by analyzing the shape and magnitude of the experimental variograms, including those from multiple spectral bands and vegetation indices, relative to other spatial intervals.

The influence of random sensor noise on CAR retrievals was examined by calculating the proportion of structural variation at multiple spatial intervals. Results indicate that systematic and random variations in CAR reflectance data are somewhat enhanced by spatial sampling effects.

This effort demonstrates a unique capability for measuring BRDF signatures, at a specific time, under the same illumination and viewing conditions, at multiple spatial scales, and with less than 2 flight-hours worth of instrument data. This new terrestrial perspective in applications of CAR airborne science data has the potential to provide further insights into the underlying sources of measurement uncertainty within merged reflectance-based products (e.g., Gao et al. (2006); Jin et al. (2002); Roy et al. (2008); van Leeuwen et al. (2006)); and to identify systematic differences between satellite sensors that may affect the quality and consistency of long-term Earth system data records.

6. References

Abdou, W.A., Helmlinger, M.C., Conel, J.E., Bruegge, C.J., Pilorz, S.H., Martonchik, J.V., & Gaitley, B.J. (2001). Ground measurements of surface BRF and HDRF using PARABOLA III. *Journal of Geophysical Research-Atmospheres*, 106, 11967-11976.

Abdou, W.A., Pilorz, S.H., Helmlinger, M.C., Conel, J.E., Diner, D.J., Bruegge, C.J., Martonchik, J.V., Gatebe, C.K., King, M.D., & Hobbs, P.V. (2006). Sua pan surface bidirectional reflectance: A case study to evaluate the effect of atmospheric correction on the

535 surface products of the Multi-angle Imaging SpectroRadiometer (MISR) during SAFARI 2000.
536 *IEEE Transactions on Geoscience and Remote Sensing*, 44, 1699-1706.

537 Atkinson, P.M. (1997). Technical note On estimating measurement error in remotely-sensed
538 images with the variogram. *International Journal of Remote Sensing*, 18, 3075-3084,
539 doi:10.1080/014311697217224.

540 Barnsley, M.J., Strahler, A.H., Morris, K.P., & Muller, J.-P. (1994). Sampling the surface
541 bidirectional reflectance distribution function (BRDF): 1. Evaluation of current and future
542 satellite sensors. *Remote Sensing Reviews*, 8, 271-311.

543 Carr, J.R., & Myers, D.E. (1984). Application of the theory of regionalized variables to the
544 spatial analysis of Landsat data. In, *Proceedings of the 9th William T. Pecora Memorial Symp on*
545 *Spatial Information Tech. for Remote Sensing Today and Tomorrow* (pp. 55-61). Los Angeles,
546 CA: IEEE.

547 Carroll, S.S., & Cressie, N. (1996). A Comparison of Geostatistical Methodologies Used to
548 Estimate Snow Water Equivalent. *Water Resources Bulletin*, 32, 267-278.

549 Chen, J.M., Leblanc, S.G., Cihlar, J.C., Bicheron, P., Leroy, M., Deering, D., & Eck, T.
550 (1997). Studies of BRDF in conifer and deciduous boreal forests using the 4-scale model and
551 airborne POLDER and ground-based PARABOLA measurements. In, *Proceedings of the IEEE*
552 *International Geoscience & Remote Sensing Symposium, IGARSS '97* (pp. 165-167). Singapore:
553 IEEE International.

554 Cohen, W.B., & Justice, C.O. (1999). Validating MODIS terrestrial ecology products:
555 Linking in situ and satellite measurements. *Remote Sensing of Environment*, 70, 1-3.

556 Curran, P.J., & Dungan, J.L. (1989). Estimation of signal to noise: a new procedure applied
557 to AVIRIS data. *IEEE Transactions on Geoscience and Remote Sensing*, 27, 620-628.

558 d'Entremont, R.P., Schaaf, C.B., & Strahler, A.H. (1996). Cloud detection and land surface
559 albedos using visible and near-infrared bidirectional reflectance distribution models. *Proceedings*
560 *of the 8th Conference on Satellite Meteorology*, 334– 338.

561 Davis, J.C. (1986). *Statistics and data analysis in geology*. New York: Wiley.

562 Deering, D.W., & Leone., P. (1986). A sphere-scanning radiometer for rapid directional
563 measurements of sky and ground radiance. *Remote Sensing of Environment*, 19, 1-24.

564 Deering, D.W., & Middleton., E. (1994). PARABOLA Data: First ISLSCP (International
565 Satellite Land Surface Climatology Project) Field Experiment (FIFE). In:

566 [<http://www.daac.ornl.gov>] from Oak Ridge National Laboratory Distributed Active Archive
 567 Center, Oak Ridge, Tennessee, U.S.A. doi:10.3334/ORNLDAAAC/68.

568 DiGirolamo, L., & Davies, R. (1994). A band-difference angular signature technique for
 569 cirrus cloud detection. *IEEE Transactions on Geoscience and Remote Sensing*, 32, 890–896.

570 Doraiswamy, P.C., Hatfield, J.L., Jackson, T.J., Akhmedov, B., Prueger, J., & Stern, A.
 571 (2004). Crop condition and yield simulations using Landsat and MODIS. *Remote Sensing of*
 572 *Environment*, 92, 548-559.

573 Friedl, M., Davis, F.W., Michaelsen, J., & Moritz, M. (1995). Scaling and uncertainty in the
 574 relationship between land surface biophysical variables and the NDVI: an analysis using a scene
 575 simulation model and data from FIFE. *Remote Sensing of Environment*, 54, 233-246.

576 Friedl, M.A., & Brodley, C.E. (1997). Decision tree classification of land cover from
 577 remotely sensed data. *Remote Sensing of Environment*, 61, 399-409.

578 Friedl, M.A., & Strahler, A.H. (2000). Mapping global land cover using the MODIS land
 579 cover classification algorithm: Recent progress and initial results. *EOS Transactions of the*
 580 *American Geophysical Union*.

581 Gao, F., Masek, J., M., S., & Hall, F. (2006). On the Blending of the Landsat and MODIS
 582 Surface Reflectance: Predict Daily Landsat Surface Reflectance. *IEEE Transactions on*
 583 *Geoscience and Remote Sensing*, 44, 2207-2218.

584 Gatebe, C.K., Butler, J.M., Cooper, J.W., Kowalewski, M., & King, M.D. (2007).
 585 Characterization of errors in the use of integrating-sphere systems in the calibration of scanning
 586 radiometers. In, *Applied Optics* (pp. 7640-7651).

587 Gatebe, C.K., Dubovik, O., & King, M.D. (2009). Simultaneous retrieval of aerosol and
 588 surface optical properties from combined airborne- and ground-based direct and diffuse
 589 radiometric measurements. *Atmospheric Chemistry and Physics Discussions*, 9, 26492-26538.

590 Gatebe, C.K., King, M.D., Lyapustin, A.I., Arnold, G.T., & Redemann, J. (2005). Airborne
 591 Spectral Measurements of Ocean Directional Reflectance. *Journal of Atmospheric Sciences*, 62,
 592 1072-1092.

593 Gatebe, C.K., King, M.D., Platnick, S., Arnold, G.T., Vermote, E.F., & Schmid, B. (2003).
 594 Airborne spectral measurements of surface-atmosphere anisotropy for several surfaces and
 595 ecosystems over southern Africa. *Journal of Geophysical Research*, 108, 1-16,
 596 doi:10.1029/2002JD002397.

597 Holben, B.N., Tanre, D., Smirnov, A., Eck, T.F., Slutsker, I., N., A., Newcomb, W.W.,
598 Schafer, J., Chatenet, B., Lavenue, F., Kaufman, Y.J., J., V.-C., Setzer, A., Markham, B., Clark,
599 D., Frouin, R., Halthore, R., Karnieli, A., O'Neill, N.T., Pietras, C., Pinker, R.T., Voss, K., &
600 Zibordi, G. (2001). An emerging ground-based aerosol climatology: Aerosol Optical Depth from
601 AERONET. *Journal of Geophysical Research*, 106, 12067-12097.

602 Huete, A., Justice, C., & Liu, H. (1994). Development of vegetation and soil indices for
603 MODIS-EOS. *Remote Sensing of Environment*, 49, 224-234.

604 Isaaks, E.H., & Srivastava, R.M. (1989). *An introduction to applied geostatistics*. New York:
605 Oxford University Press.

606 Jackson, T.J., Chen, D., Cosh, M.H., Li, F., Anderson, M., Walthall, C., Doraiswamy, P., &
607 Hunt, E.R. (2004). Vegetation water content mapping using Landsat data derived normalized
608 difference water index for corn and soybeans. *Remote Sensing of Environment*, 92, 475-482.

609 Jin, Y., Schaaf, C.B., Gao, F., Li, X., Strahler, A.H., Bruegge, C., & Martonchik, J. (2002).
610 Improving MODIS surface BRDF/Albedo retrieval with MISR multi-angle observations. *IEEE*
611 *Transactions on Geoscience and Remote Sensing*, 40, 1593-1604.

612 Jupp, D.L.B., Strahler, A.H., & Woodcock, C.E. (1988). Autocorrelation and regularization
613 in digital images. I - Basic theory. *IEEE Transactions on Geoscience and Remote Sensing*, 26,
614 463-473.

615 Jupp, D.L.B., Strahler, A.H., & Woodcock, C.E. (1989). Autocorrelation and regularization
616 in digital images. II. Simple image models. *IEEE Transactions on Geoscience and Remote*
617 *Sensing*, 27, 247-258.

618 Kaufman, Y.J. (1989). The atmospheric effect on remote sensing and its correction. In G.
619 Asrar (Ed.), *Theory and Applications of Optical Remote Sensing* (pp. 336-428). New York: John
620 Wiley.

621 King, M.D. (1981). A method for determining the single scattering albedo of clouds through
622 observation of the internal scattered radiation field. *Journal of Atmospheric Sciences*, 38, 2031-
623 2044.

624 King, M.D., Radke, L.F., & Hobbs, P.V. (1990). Determination of the spectral absorption of
625 solar radiation by marine stratocumulus clouds from airborne measurements within clouds.
626 *Journal of Atmospheric Sciences*, 47, 894-907.

627 King, M.D., Strange, M.G., Leone, P., & Blaine, L.R. (1986). Multiwavelength scanning
628 radiometer for airborne measurements of scattered radiation within clouds. *Journal of*
629 *Atmospheric and Oceanic Technology*, 3, 513-522.

Knobelspiesse, K.D., Cairns, B., Schmid, B., Román, M., & Schaaf, C.B. (2008). Surface BRDF estimation from an aircraft compared to MODIS and ground estimates at the Southern Great Plains site. *Journal of Geophysical Research-Atmospheres*, 113, D20, doi:10.1029/2008JD010062.

Kotchenova, S.Y., Vermote, E.F., Matarrese, R., & Klemm, F.J. (2006). Validation of a vector version of the 6S radiative transfer code for atmospheric correction of satellite data. Part I: Path Radiance. *Applied Optics*, 45, 6726-6774.

Leroy, M., Deuzé, J.L., Bréon, F.M., Hautecoeur, O., Herman, M., Buriez, J.C., Tanré, D., Bouffié, S., Chazette, P., & Roujean, J.-L. (1997). Retrieval of atmospheric properties and surface bidirectional reflectances over land from POLDER/ADEOS. *Journal of Geophysical Research*, 102, 17023-17037.

Leroy, M., & Hautecoeur, O. (1999). Anisotropy-corrected vegetation indexes derived from POLDER ADEOS. *IEEE Transactions on Geoscience and Remote Sensing*, 37, 1698-1708.

Li, H., & Reynolds, J.E. (1995). On definition and quantification of heterogeneity. *Oikos: A Journal of Ecology*, 73, 280-284.

Li, X.W., & Strahler, A.H. (1992). Geometric-Optical Bidirectional Reflectance Modeling of the Discrete Crown Vegetation Canopy - Effect of Crown Shape and Mutual Shadowing. *IEEE Transactions on Geoscience and Remote Sensing*, 30, 276-292.

Li, Z., Cihlar, J., Zheng, X., Moreau, L., & Ly, H. (1996). The bidirectional effects of AVHRR measurements over boreal regions. *IEEE Transactions on Geoscience and Remote Sensing*, 34, 1308-1322.

Liang, S., Fang, H.L., Chen, M.Z., Shuey, C.J., Walthall, C., Daughtry, C., Morisette, J., Schaaf, C.B., & Strahler, A.H. (2002). Validating MODIS land surface reflectance and albedo products: methods and preliminary results. *Remote Sensing of Environment*, 83, 149-162.

Lucht, W., Schaaf, C.B., & Strahler, A.H. (2000). An algorithm for the retrieval of albedo from space using semi-empirical BRDF models. *IEEE Transactions on Geoscience and Remote Sensing*, 38, 977-998.

Materon, G. (1963). Principles of Geostatistics. *Economic Geology*, 58, 1246-1266, DOI: 10.2113/gsecongeo.58.8.1246.

Morisette, J., F. Baret, Myneni, R.B., Nickeson, J.E., & et. al. (2006). Validation of Global Moderate-Resolution LAI products: A Framework Proposed Within the CEOS Land Product Validation Subgroup. 44, 7, 1804-1817.

- 662 Nicodemus, F.E. (1977). Geometrical considerations and nomenclature for reflectance.
663 *National Bureau of Standards monograph, no. 160* (pp. 1-52). Washington, DC.
- 664 Privette, J.L., Morisette, J.T., Myneni, R.B., & Justice, C.O. (1998). Global Validation of
665 EOS LAI and FPAR Products. *The Earth Observer*, 10, 39-42.
- 666 Rastetter, E.B., King, A.W., Cosby, B.J., Hornberger, G.M., O'neil, R.V., & Hobbie, J.E.
667 (1992). Aggregating fine-scale ecological knowledge to model coarser-scale attributes of
668 ecosystems. *Ecological Applications*, 2, 55-70.
- 669 Román, M., Schaaf, C.B., Lewis, P., Gao, F., Anderson, G.P., Privette, J.L., Strahler, A.H.,
670 Woodcock, C.E., & Barnsley, M. (2010). Assessing the Coupling between Surface Albedo
671 derived from MODIS and the Fraction of Diffuse Skylight over Spatially-Characterized
672 Landscapes. *Remote Sensing of Environment*, 114, 738-760, doi:10.1016/j.rse.2009.11.014.
- 673 Román, M.O., Schaaf, C.B., Yang, X., Woodcock, C.E., Strahler, A.H., Braswell, R.H.,
674 Curtis, P.S., Davis, K.J., D., D., Gu, L., Goulden, M.L., Hollinger, D.Y., Kolb, T.E., Meyers,
675 T.P., Munger, J.W., Privette, J.L., Richardson, A.D., Wilson, T.B., & Wofsy, S.C. (2009). The
676 MODIS (Collection V005) BRDF/albedo product: Assessment of spatial representativeness over
677 forested landscapes. *Remote Sensing of Environment*, 113, 2476-2498,
678 10.1016/j.rse.2009.07.009.
- 679 Ross, J. (1981). *The radiation regime and architecture of plant stands*. Norwell, Mass.: The
680 Hague: Dr. W. Junk Publishers.
- 681 Roujean, J.-L., Leroy, M., Podaire, A., & Deschamps, P.Y. (1992). Evidence of Surface
682 Reflectance Bidirectional Effects from a Noaa/Avhrr Multitemporal Data Set. *International*
683 *Journal of Remote Sensing*, 13, 685-698.
- 684 Roy, D.P., Ju, J., Lewis, P., Schaaf, C.B., Gao, F., Hansen, M., & Lindquist, E. (2008).
685 Multi-temporal MODIS–Landsat data fusion for relative radiometric normalization, gap filling,
686 and prediction of Landsat data *Remote Sensing of Environment*, 112, 3112-3130.
- 687 Schaaf, C.B., Gao, F., Strahler, A.H., Lucht, W., Li, X., Tsang, T., Strugnell, N.C., Zhang,
688 X., Jin, Y., Muller, J.-P., Lewis, P., Barnsley, M., Hobson, P., Disney, M., Roberts, G.,
689 Dunderdale, M., Doll, C., d'Entremont, R., Hu, B., Liang, S., Privette, J.L., & Roy, D.P. (2002).
690 First Operational BRDF, Albedo and Nadir Reflectance Products from MODIS. *Remote Sensing*
691 *of Environment*, 83, 135-148.
- 692 Schaepman-Strub, G., Schaepman, M.E., Painter, T.H., Dangel, S., & Martonchik, J.V.
693 (2006). Reflectance quantities in optical remote sensing-definitions and case studies. *Remote*
694 *Sensing of Environment*, 103, 27-42.

695 Shuai, Y., Schaaf, C.B., Strahler, A.H., Liu, J., & Jiao, Z. (2008). Quality assessment of
696 BRDF/albedo retrievals in MODIS operational system. *Geophysical Research Letters*, 35,
697 L05407.

698 Strahler, A.H., Lucht, W., Schaaf, C.B., Tsang, T., Gao, F., Li, X., Muller, J.-P., Lewis, P.,
699 & Barnsley, M. (1999). MODIS BRDF/Albedo Product: Algorithm Theoretical Basis Document
700 Version 5.0. Technical Report. In: NASA EOS-MODIS.

701 Strahler, A.H., Townshend, J.T., Muchoney, D., Borak, J.S., Friedl, M.A., Gopal, S.,
702 Hyman, A., Moody, A., & Lambin, E. (1996). MODIS land cover and land cover change:
703 Algorithm technical basis document. In (p. 120): NASA EOS-MODIS.

704 Susaki, J., Hara, K., Park, J.G., Yasuda, Y., Kajiwara, K., & Honda, Y. (2004). Validation of
705 temporal BRDFs of paddy fields estimated from MODIS reflectance data. *IEEE Transactions on*
706 *Geoscience and Remote Sensing*, 42, 1262-1270.

707 Susaki, J., Yasuoka, Y., Kajiwara, K., Honda, Y., & Hara, K. (2007). Validation of MODIS
708 albedo products of paddy fields in Japan. *IEEE Transactions on Geoscience and Remote*
709 *Sensing*, 45, 206-217.

710 Tucker, C.J. (1979). Red and photographic infrared linear combinations for monitoring
711 vegetation. *Remote Sensing of Environment*, 8, 127-150.

712 van Leeuwen, W.J.D., Orr, B.J., Marsh, S.E., & Herrmann, S.M. (2006). Multi-sensor NDVI
713 data continuity: Uncertainties and implications for vegetation monitoring applications. *Remote*
714 *Sensing of Environment*, 100, 67-81.

715 Wanner, W., Li, X., & Strahler, A.H. (1995). On the Derivation of Kernels for Kernel-
716 Driven Models of Bidirectional Reflectance. *Journal of Geophysical Research-Atmospheres*,
717 100, 21077-21089.

718 Wanner, W., Strahler, A.H., Hu, B., Lewis, P., Muller, J., Li, X., Schaaf, C.B., & Barnsley,
719 M. (1997). Global retrieval of bidirectional reflectance and albedo over land from EOS MODIS
720 and MISR data: Theory and algorithm. *Journal of Geophysical Research*, 102, 17143-17161.

721 Wenge, N., & Xiaowen, L. (2000). A coupled vegetation-soil bidirectional reflectance model
722 for a semiarid landscape. *Remote Sensing of Environment*, 74, 113-124.

723 Woodcock, C.E., & Strahler, A.H. (1987). The Factor of Scale in Remote Sensing. *Remote*
724 *Sensing of Environment*, 21, 311-342.

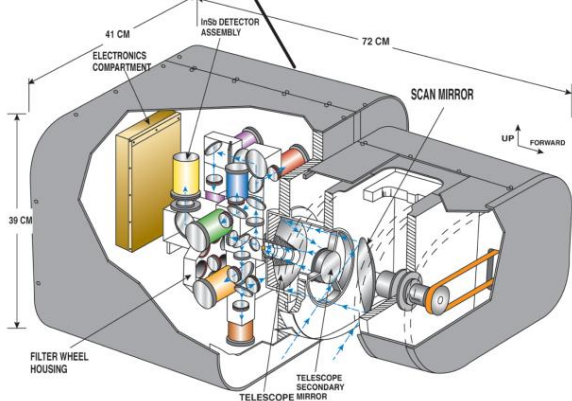
725 Woodcock, C.E., Strahler, A.H., & Jupp, D.L.B. (1988). The Use of Variograms in Remote
726 Sensing: II Real Digital Images. *Remote Sensing of Environment*, 25, 349-379.

727 WWW1. NASA: Cloud Absorption Radiometer (2009). <http://car.gsfc.nasa.gov/>.
728 Zhang, X., Friedl, M., & Schaaf, C. (2009). Sensitivity of vegetation phenology detection to
729 the temporal resolution of satellite data. *International Journal of Remote Sensing*, 30, 2061-2074.
730
731
732

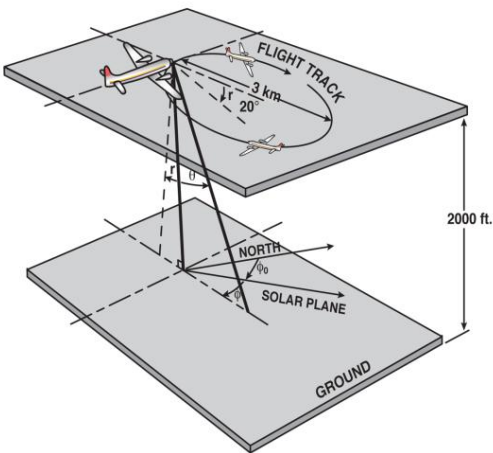
a. Jetstream-31 Aircraft



b. CAR Schematic



c. BRDF Flight Track



d. Cloud Absorption Radiometer (CAR) Parameters

| | |
|--|---|
| Angular scan range | 190° |
| Instantaneous field of view | 17.5 mrad (1°) |
| Pixels per scan line | 382 |
| Scan rate | 1.67 scan lines per second (100 rpm) |
| Spectral channels (μm; bandwidth (FWHM)) | 14 ^a (8 continuously sampled and last six in filter wheel): 0.340(0.009), 0.381(0.006), 0.472(0.021), 0.682(0.022), 0.870(0.022), 1.036(0.022), 1.219(0.022), 1.273(0.023), 1.556(0.032), 1.656(0.045), 1.737(0.040), 2.103(0.044), 2.205(0.042), 2.302(0.043) |

Fig. 1. (a.) The N22746 aircraft registered to Sky Research Inc. (USA), also known as Jetstream-31 (J-31) in Ponca City Airport, Oklahoma, USA during the 2007 Cloud and Land Surface Interaction Campaign (CLASIC). (b.) Schematic of NASA's Cloud Absorption Radiometer (CAR), which is mounted in the nose cone of the J-31. The CAR measured the spectral and angular distribution of scattered light by clouds and aerosols, and obtained good imagery of clouds and Earth surface features over many areas in the Southern Great Plains (SGP). (c.) Illustration of a clockwise circular flight track that was used for measuring surface bidirectional reflectance distribution function (BRDF) over the SGP Central Facility during CLASIC. (d.) The CAR has 14 narrow spectral bands between 0.34 and 2.30 μm, and flew 11 missions during CLASIC. (Gatebe et al., 2003; King et al., 1986).

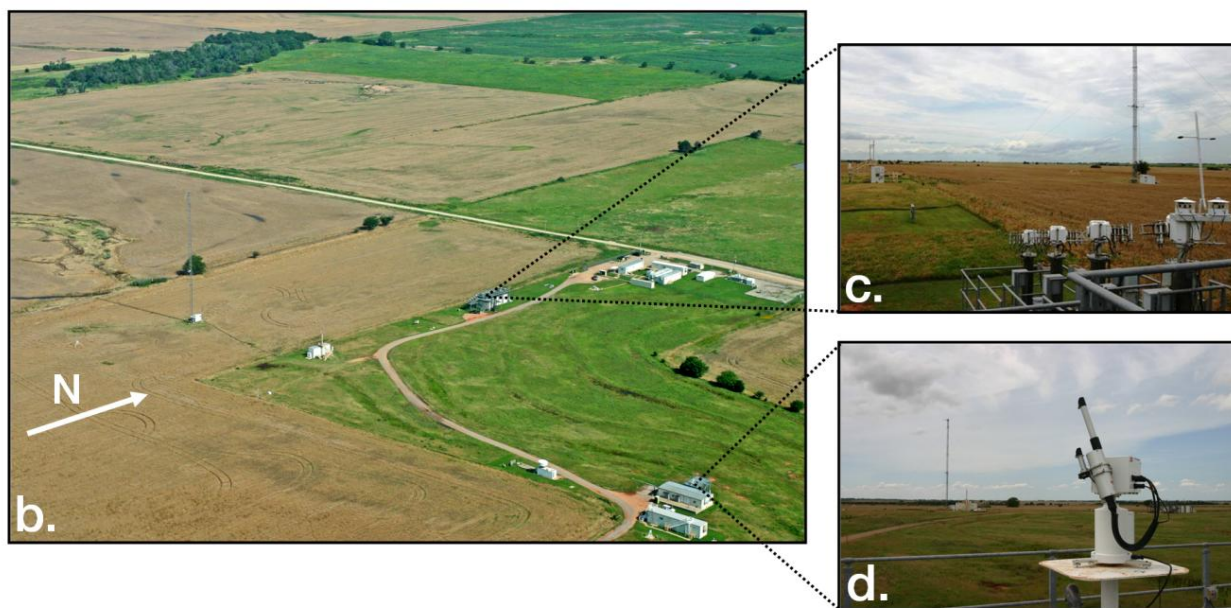
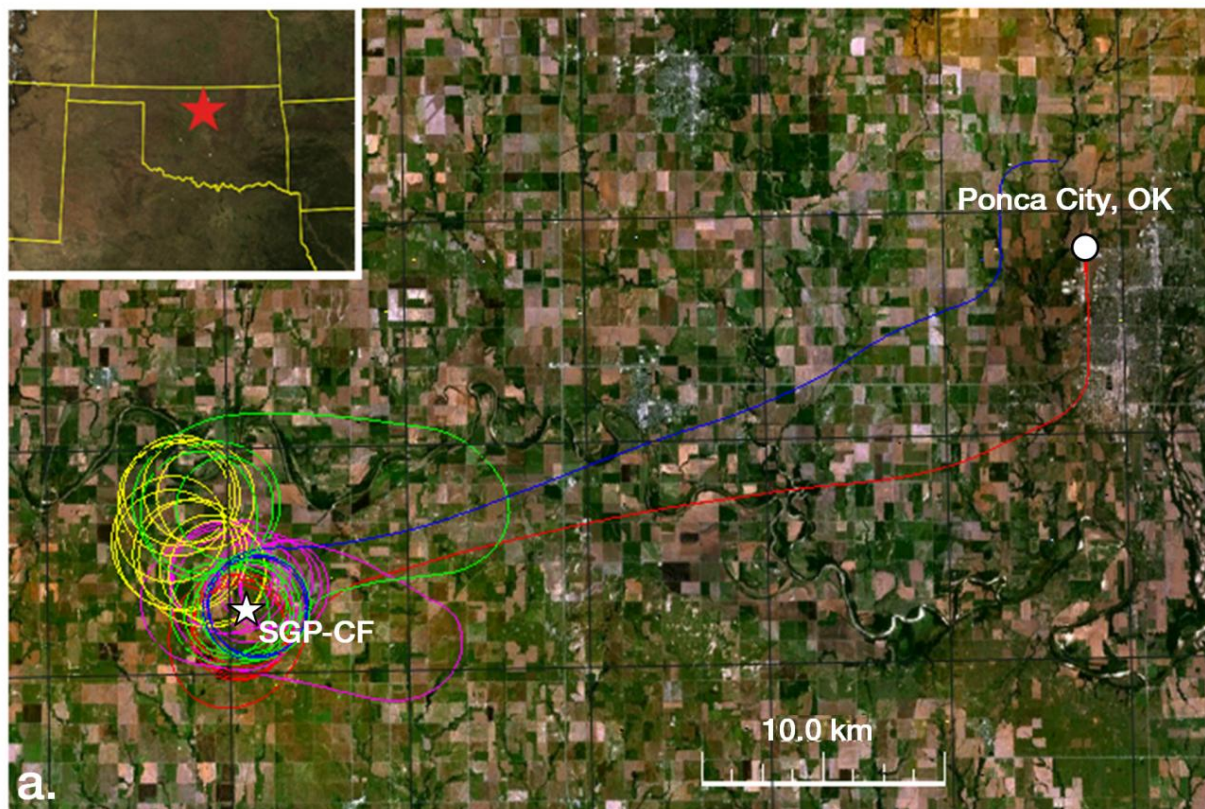
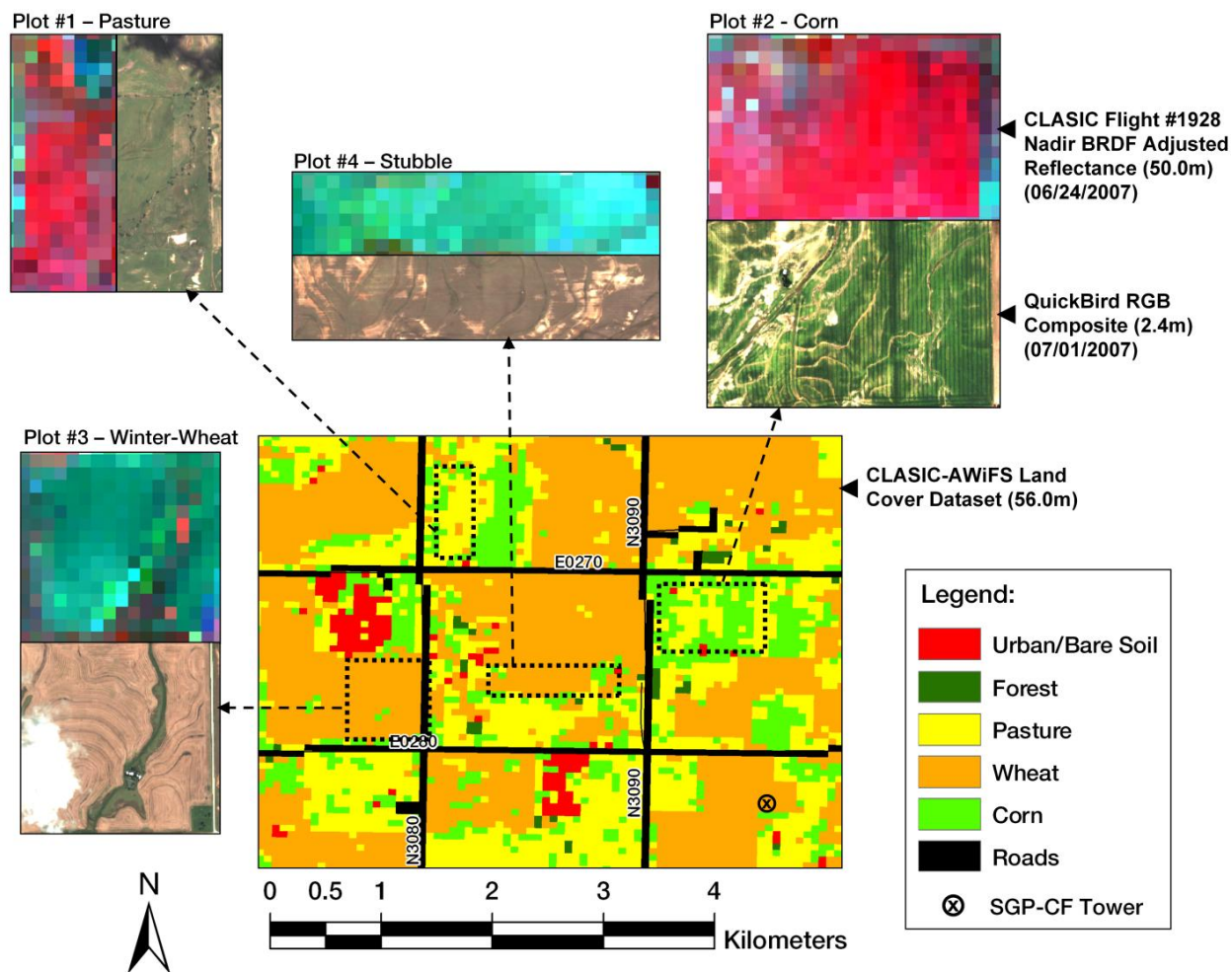


Figure 2. (a.) CLASIC-Flight #1928 flight track over the ARM Program's Southern Great Plains Central Facility (SGP-CF) (24 June 2007). The multi-colored track shows the time sequence, with red representing the first 30 minutes of the flight, and then a series of 14-minute time steps starting with magenta, yellow, green, and blue. (b.) Bird's eye view of the SGP-CF taken during CLASIC Flight #1922 (19 June 2007). (c.) Facing southwest atop the Radiometric Calibration Facility, overlooking the upward-facing pyranometers and the 60 meter radiation tower (20 June 2007). (d.) Facing west atop the Guest Instrument Facility, overlooking the AERONET sun photometer (20 June 2007).

24
25
26



27
28 Fig 3. CLASIC-AWiFS land cover subset indicating the study plots (dashed rectangles) that were sampled by the
29 CAR instrument during CLASIC Flight #1928; and the location of the 60 m flux-tower at the ARM-SGP Central
30 Facility ("X" mark). Each plot display consists of: (1) 50m Nadir BRDF Adjusted Reflectance (NBAR) subsets
31 (RGB = NIR, Red, Blue) obtained from RTLSR BRDF model inversions of each CAR pixel; and (2) True-color
32 subsets from a 2.4 m QuickBird scene acquired just 7 days after CLASIC Flight #1928 (1 July 2007).
33
34
35
36
37
38
39
40
41
42
43
44
45
46
47
48

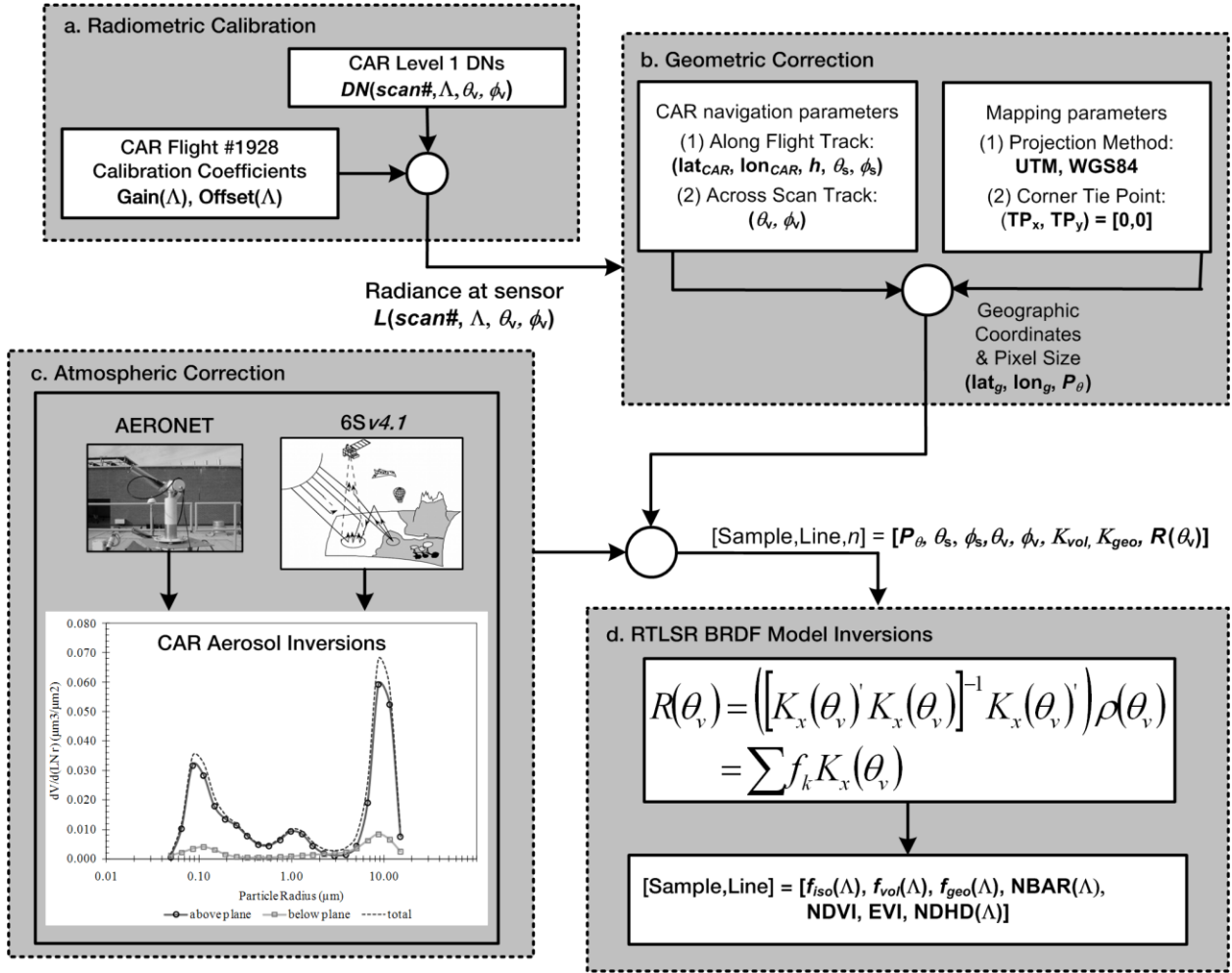


Fig. 4. Processing and data flow diagram illustrating the production of areal-mean, nadir-normalized, and angular indexes of vegetation structure from CAR observations. (c.) Aerosol column particle volume size distribution retrieved from the CAR at an altitude of 200 m above ground level at the SGP-CF during CLASIC Flight #1928 on 24 June 2007.

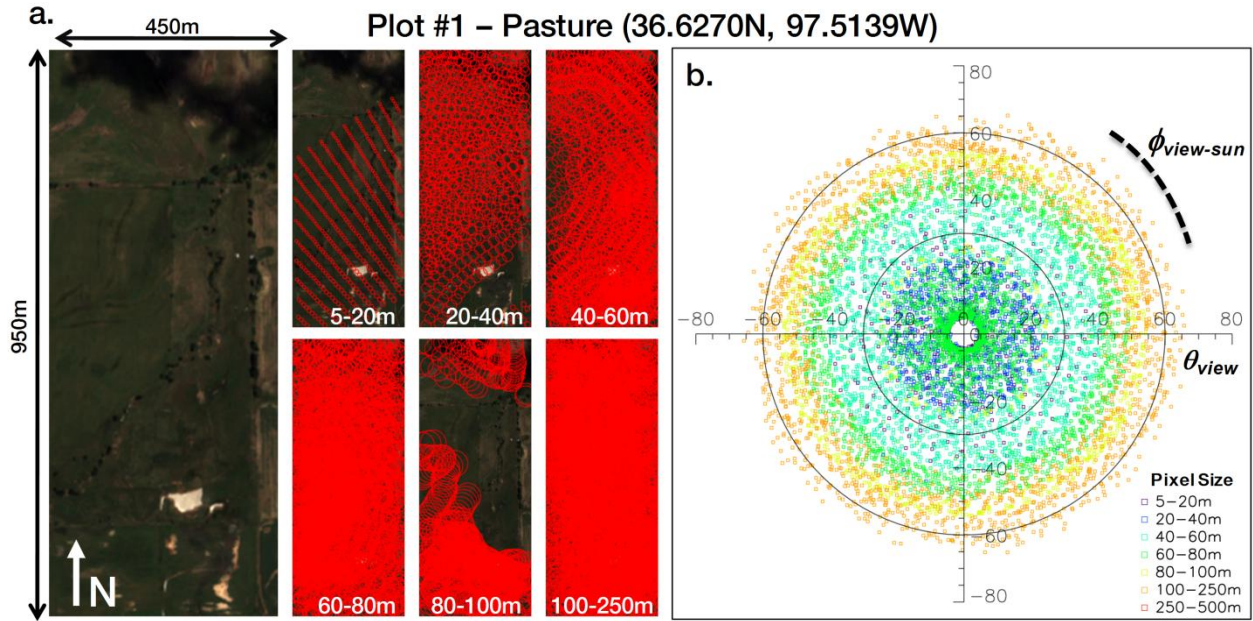


Fig. 5. (a.) Spatial Distribution of BRF retrievals from CAR at 6 spatial intervals over a plot of pasture located outside of Lamont, Oklahoma. (b.) Polar plot showing the angular distribution of the BRF using the same observations and spatial intervals as Fig. 5a.

Table 1. Plot #1 - Pasture (Fig. 5). Summary and multi-scale comparisons between: (1) areal-mean estimates of surface directional reflectance and Nadir-BRDF Adjusted Reflectances (cf. RTLSR Model: NBAR) for CAR bands #3, #4, and #5; (2) at-nadir and (3) areal-mean estimates of NDVI and EVI compared against NBAR retrievals.

| Sample Size | Scan Angle (Mean \pm Stdev) | Pixel Size (Mean \pm Stdev) | Direct Method: Mean BRFs | | | Direct Method: Vegetation Indexes | | | |
|--|----------------------------------|----------------------------------|--------------------------|--------------------|-------------------|-----------------------------------|--------------------------------------|-------------------|-------------------|
| | | | Band3 | Band4 | Band5 | NDVI@nadir | EVI@nadir | Mean NDVI | Mean EVI |
| 488 | 19.22° \pm 11.51° | 13.09 \pm 2.25m | 0.0377 | 0.0648 | 0.4029 | 0.7386 | 0.5753 | 0.7753 | 0.6487 |
| 842 | 16.54° \pm 5.89° | 36.62 \pm 2.59m | 0.0409 | 0.0709 | 0.3869 | 0.7320 | 0.5875 | 0.6792 | 0.5257 |
| 1683 | 32.81° \pm 5.37° | 50.64 \pm 6.53m | 0.0385 | 0.0678 | 0.4046 | 0.7336 | 0.5804 | 0.6977 | 0.5756 |
| 2484 | 28.07° \pm 17.09° | 68.9 \pm 4.86m | 0.0440 | 0.0793 | 0.3918 | 0.7341 | 0.5793 | 0.6748 | 0.5652 |
| 804 | 49.30° \pm 8.71° | 89.73 \pm 6.02m | 0.0411 | 0.0711 | 0.3960 | 0.7378 | 0.5717 | 0.6831 | 0.5873 |
| 1779 | 54.49° \pm 5.57° | 135.97 \pm 23.45m | 0.0364 | 0.0650 | 0.3829 | 0.7612 | 0.6241 | 0.5840 | 0.5159 |
| Pixel Size (Mean \pm Stdev) | RTLSR Model Uncertainty | | | RTLSR Model: NBAR | | | RTLSR Model: NBAR Vegetation Indexes | | |
| | Band3 | Band4 | Band5 | Band3 | Band4 | Band5 | NBAR-NDVI | NBAR-EVI | NBAR-NDVI |
| 13.09 \pm 2.25m | 0.0027 | 0.0059 | 0.0261 | 0.0291 | 0.0483 | 0.3050 | 0.7266 | 0.4662 | 0.7266 |
| 36.62 \pm 2.59m | 0.0030 | 0.0064 | 0.0281 | 0.0321 | 0.0529 | 0.3009 | 0.7010 | 0.4501 | 0.7010 |
| 50.64 \pm 6.53m | 0.0040 | 0.0063 | 0.0288 | 0.0305 | 0.0493 | 0.3120 | 0.7271 | 0.4762 | 0.7271 |
| 68.9 \pm 4.86m | 0.0050 | 0.0076 | 0.0287 | 0.0309 | 0.0540 | 0.3150 | 0.7073 | 0.4637 | 0.7073 |
| 89.73 \pm 6.02m | 0.0038 | 0.0066 | 0.0284 | 0.0310 | 0.0511 | 0.3220 | 0.7261 | 0.4851 | 0.7261 |
| 135.97 \pm 23.45m | 0.0027 | 0.0053 | 0.0283 | 0.0300 | 0.0520 | 0.3120 | 0.7143 | 0.4646 | 0.7143 |
| Accuracy Assessment | | | Band3 | Band4 | Band5 | NBAR-NDVI | NBAR-EVI | NBAR-NDVI | NBAR-EVI |
| Measurement uncertainty without BRDF correction (Abs. / Rel.) | | | 0.0041 / 9.48% | 0.0086 / 11.23% | 0.0079 / 2.01% | 0.0110 / 1.50% | 0.0192 / 3.31% | 0.0564 / 8.16% | 0.0446 / 7.71% |
| Measurement uncertainty with BRDF correction (Abs. / Rel.) | | | 0.0009 / 3.02% | 0.0027 / 5.03% | 0.0071 / 2.28% | 0.0122 / 1.72% | 0.0115 / 2.47% | 0.0122 / 1.72% | 0.0115 / 2.47% |

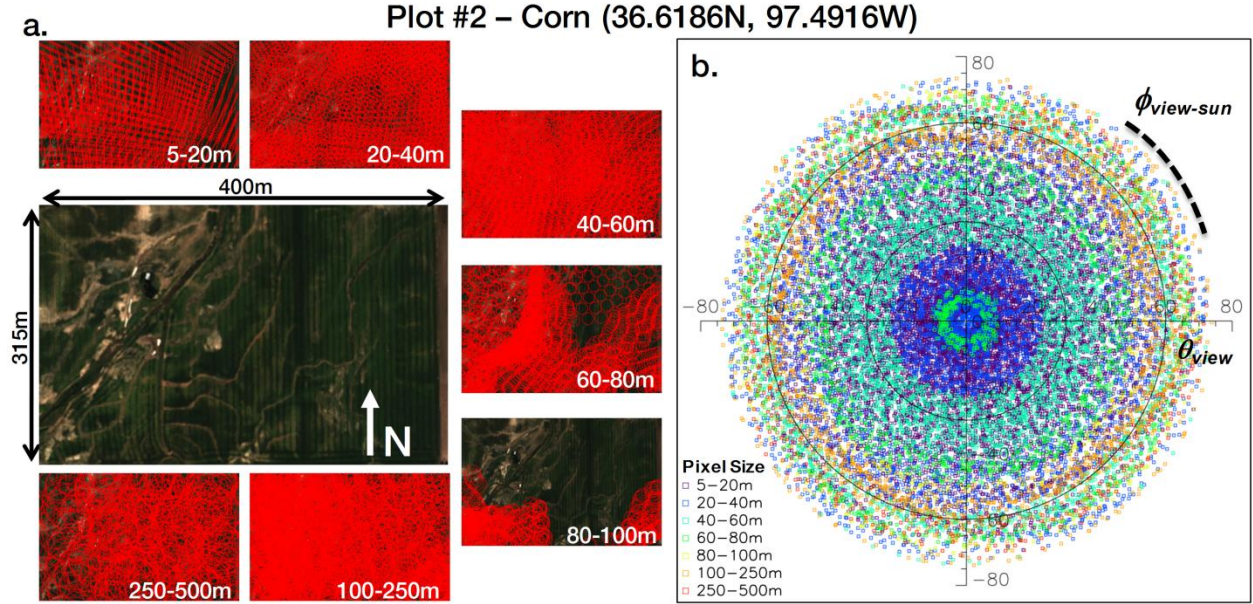


Fig. 6. (a.) Spatial Distribution of BRF retrievals from CAR at 7 spatial intervals over a plot of corn located outside of Lamont, Oklahoma. (b.) Polar plot showing the angular distribution of the BRF using the same spatial intervals as Fig. 6a.

Table 2. Summary statistics and multi-scale comparisons for Plot #2 - Corn (Fig. 6). Setup is the same as Table 1.

| Sample Size | Mean Scan Angle | Pixel Size (Mean ± Stdev) | | Direct Method: Mean BRFs | | | Direct Method: Vegetation Indexes | | | |
|--|-------------------------|------------------------------|--------|--------------------------|--------------------|--------------------|--------------------------------------|--------------------|--------------------|--------------------|
| | | | | Band3 | Band4 | Band5 | NDVI@nadir | EVI@nadir | Mean NDVI | Mean EVI |
| 13102 | 27.46° ± 17.68° | 7.44 ± 4.74m | | 0.0415 | 0.0648 | 0.4165 | 0.7617 | 0.5678 | 0.7710 | 0.5900 |
| 4454 | 39.33° ± 22.26° | 31.54 ± 5.96m | | 0.0314 | 0.0535 | 0.3356 | 0.7257 | 0.4131 | 0.7520 | 0.6490 |
| 3948 | 41.56° ± 14.82° | 48.33 ± 5.49m | | 0.0286 | 0.0492 | 0.3290 | 0.7556 | 0.4941 | 0.7394 | 0.6838 |
| 1784 | 47.22° ± 18.27° | 68.76 ± 5.38m | | 0.0232 | 0.0426 | 0.2394 | 0.7019 | 0.3804 | 0.7513 | 0.7112 |
| 485 | 58.07° ± 8.60° | 87.7 ± 5.90m | | 0.0260 | 0.0485 | 0.2227 | 0.6452 | 0.3280 | 0.7181 | 0.7301 |
| 1884 | 60.09° ± 5.42° | 152.29 ± 42.95m | | 0.0241 | 0.0442 | 0.2418 | 0.7347 | 0.4009 | 0.5354 | 0.5214 |
| 390 | 64.79° ± 3.50° | 286.27 ± 25.79m | | 0.0242 | 0.0448 | 0.2141 | 0.6043 | 0.3194 | 0.5164 | 0.4439 |
| Pixel Size (Mean ± Stdev) | RTLSR Model Uncertainty | | | RTLSR Model: NBAR | | | RTLSR Model: NBAR Vegetation Indexes | | | |
| | Band3 | Band4 | Band5 | Band3 | Band4 | Band5 | NBAR-NDVI | NBAR-EVI | NBAR-NDVI | NBAR-EVI |
| 7.44 ± 4.74m | 0.0098 | 0.0183 | 0.0396 | 0.0250 | 0.0404 | 0.3370 | 0.7857 | 0.5399 | 0.7857 | 0.5399 |
| 31.54 ± 5.96m | 0.0064 | 0.0145 | 0.0232 | 0.0249 | 0.0399 | 0.3052 | 0.7689 | 0.4971 | 0.7689 | 0.4971 |
| 48.33 ± 5.49m | 0.0054 | 0.0125 | 0.0264 | 0.0263 | 0.0434 | 0.2876 | 0.7379 | 0.4629 | 0.7379 | 0.4629 |
| 68.76 ± 5.38m | 0.0042 | 0.0093 | 0.0085 | 0.0286 | 0.0473 | 0.3348 | 0.7523 | 0.5237 | 0.7523 | 0.5237 |
| 87.7 ± 5.90m | 0.0047 | 0.0091 | 0.0051 | 0.0279 | 0.0531 | 0.2290 | 0.6237 | 0.3456 | 0.6237 | 0.3456 |
| 152.29 ± 42.95m | 0.0047 | 0.0101 | 0.0090 | 0.0320 | 0.0525 | 0.3377 | 0.7311 | 0.5171 | 0.7311 | 0.5171 |
| 286.27 ± 25.79m | 0.0038 | 0.0075 | 0.0043 | 0.0211 | 0.0373 | 0.2848 | 0.7685 | 0.4709 | 0.7685 | 0.4709 |
| Accuracy Assessment | | | | Band3 | Band4 | Band5 | NBAR-NDVI | NBAR-EVI | NBAR-NDVI | NBAR-EVI |
| Measurement uncertainty without BRDF correction (Abs. / Rel.) | | | | 0.0096 / 26.76% | 0.0112 / 19.13% | 0.1119 / 30.03% | 0.0707 / 9.44% | 0.1270 / 24.84% | 0.1269 / 16.69% | 0.0981 / 15.66% |
| Measurement uncertainty with BRDF correction (Abs. / Rel.) | | | | 0.0034 / 13.15% | 0.0068 / 16.40% | 0.0418 / 12.97% | 0.0602 / 7.80% | 0.0713 / 13.79% | 0.0602 / 7.80% | 0.0713 / 13.79% |

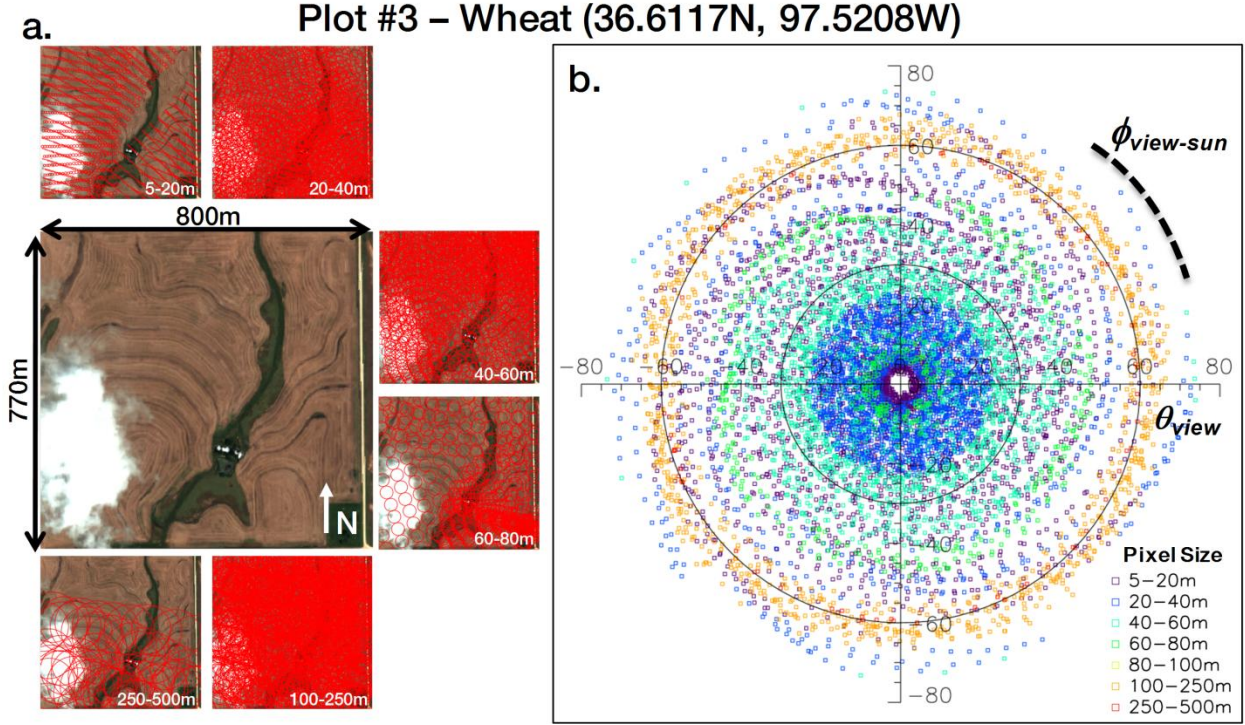


Fig. 7. (a.) Spatial Distribution of BRF retrievals from CAR at 6 spatial intervals over a plot of winter-wheat located outside of Lamont, Oklahoma. (b.) Polar plot showing the angular distribution of the BRF using the same spatial intervals as Fig. 7a.

Table 3. Summary statistics and multi-scale comparisons for Plot #3 - Wheat (Fig. 7). Setup is the same as Table 1.

| Sample Size | Mean Scan Angle | Pixel Size (Mean ± Stdev) | | Direct Method: Mean BRFs | | | Direct Method: Vegetation Indexes | | | |
|--|-------------------------|------------------------------|--------|--------------------------|--------------------|--------------------|--------------------------------------|--------------------|--------------------|--------------------|
| | | | | Band3 | Band4 | Band5 | NDVI@nadir | EVI@nadir | Mean NDVI | Mean EVI |
| 3141 | 29.05° ± 17.66° | 7.12 ± 4.77m | | 0.0513 | 0.1048 | 0.1945 | 0.3013 | 0.1687 | 0.3304 | 0.1533 |
| 2596 | 22.83° ± 17.11° | 34.93 ± 4.61m | | 0.0473 | 0.0965 | 0.1842 | 0.3178 | 0.1749 | 0.3716 | 0.2423 |
| 1830 | 27.99° ± 8.75° | 46.95 ± 5.24m | | 0.0408 | 0.0819 | 0.1543 | 0.3057 | 0.1347 | 0.3639 | 0.2383 |
| 505 | 34.26° ± 16.62° | 67.32 ± 4.41m | | 0.0238 | 0.0508 | 0.0937 | 0.2826 | 0.0962 | 0.3784 | 0.2623 |
| 1006 | 61.41° ± 2.96° | 174.96 ± 32.78m | | 0.0281 | 0.0605 | 0.1081 | 0.3215 | 0.0994 | 0.3177 | 0.2790 |
| 65 | 59.36° ± 0.43° | 260.07 ± 6.78m | | 0.0267 | 0.0598 | 0.1055 | 0.2934 | 0.0978 | 0.2478 | 0.1925 |
| Pixel Size (Mean ± Stdev) | RTLSR Model Uncertainty | | | RTLSR Model: NBAR | | | RTLSR Model: NBAR Vegetation Indexes | | | |
| | Band3 | Band4 | Band5 | Band3 | Band4 | Band5 | NBAR-NDVI | NBAR-EVI | NBAR-NDVI | NBAR-EVI |
| 7.12 ± 4.77m | 0.0178 | 0.0253 | 0.0459 | 0.0320 | 0.0795 | 0.1486 | 0.3027 | 0.1406 | 0.3027 | 0.1406 |
| 34.93 ± 4.61m | 0.0138 | 0.0214 | 0.0438 | 0.0319 | 0.0752 | 0.1404 | 0.3026 | 0.1342 | 0.3026 | 0.1342 |
| 46.95 ± 5.24m | 0.0083 | 0.0140 | 0.0305 | 0.0294 | 0.0616 | 0.1189 | 0.3171 | 0.1214 | 0.3171 | 0.1214 |
| 67.32 ± 4.41m | 0.0004 | 0.0007 | 0.0033 | 0.0209 | 0.0435 | 0.0901 | 0.3487 | 0.1027 | 0.3487 | 0.1027 |
| 174.96 ± 32.78m | 0.0024 | 0.0055 | 0.0118 | 0.0236 | 0.0493 | 0.0886 | 0.2852 | 0.0865 | 0.2852 | 0.0865 |
| 260.07 ± 6.78m | 0.0005 | 0.0012 | 0.0013 | 0.0262 | 0.0586 | 0.1042 | 0.2801 | 0.0980 | 0.2801 | 0.0980 |
| Accuracy Assessment | | | | Band3 | Band4 | Band5 | NBAR-NDVI | NBAR-EVI | NBAR-NDVI | NBAR-EVI |
| Measurement uncertainty without BRDF correction (Abs. / Rel.) | | | | 0.0154 / 32.43% | 0.0293 / 30.16% | 0.0578 / 31.77% | 0.0137 / 4.47% | 0.0496 / 29.99% | 0.0476 / 13.55% | 0.0515 / 25.86% |
| Measurement uncertainty with BRDF correction (Abs. / Rel.) | | | | 0.0056 / 17.97% | 0.0187 / 24.94% | 0.0343 / 24.44% | 0.0226 / 7.39% | 0.0287 / 21.29% | 0.0226 / 7.39% | 0.0287 / 21.29% |

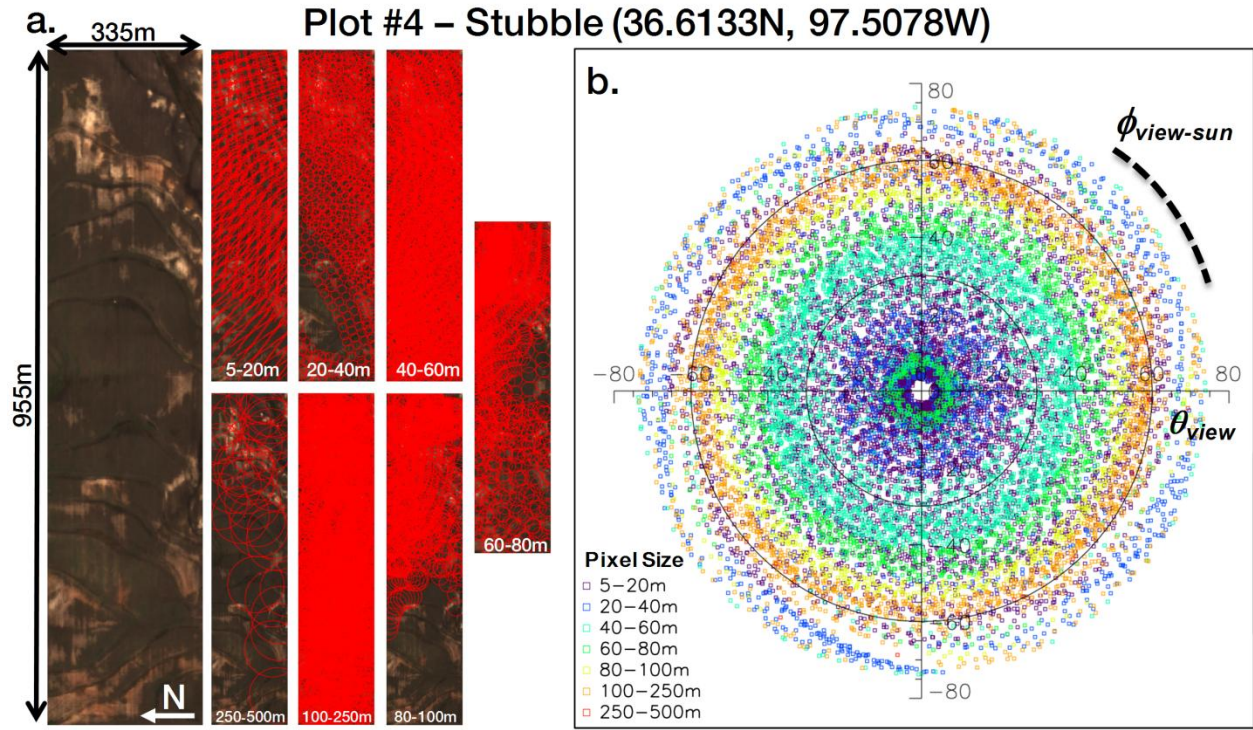


Fig. 8. (a.) Spatial Distribution of BRF retrievals from CAR at 7 spatial intervals over a plot of stubble land located outside of Lamont, Oklahoma. (b.) Polar plot showing the angular distribution of the BRF using the same spatial intervals as Fig. 8a.

Table 4. Summary statistics and multi-scale comparisons for Plot #4 - Stubble (Fig. 8). Setup is the same as Table 1.

| Sample Size | Mean Scan Angle | Pixel Size (Mean ± Stdev) | Direct Method: Mean BRFs | | | Direct Method: Vegetation Indexes | | | | |
|--|-------------------------|------------------------------|--------------------------|--------------------|--------------------|-----------------------------------|--------------------------------------|-------------------|--------------------|--------------------|
| | | | Band3 | Band4 | Band5 | NDVI@nadir | EVI@nadir | Mean NDVI | Mean EVI | |
| 7523 | 29.75° ± 19.14° | 7.09 ± 4.39m | 0.0554 | 0.1263 | 0.2318 | 0.3016 | 0.1633 | 0.2892 | 0.1565 | |
| 1425 | 46.37° ± 25.23° | 31.53 ± 6.16m | 0.0382 | 0.0860 | 0.1600 | 0.2899 | 0.1547 | 0.2944 | 0.2083 | |
| 2954 | 34.61° ± 11.20° | 50.38 ± 5.56m | 0.0556 | 0.1258 | 0.2278 | 0.2894 | 0.1673 | 0.3158 | 0.2192 | |
| 1424 | 41.91° ± 12.83° | 67.81 ± 5.47m | 0.0431 | 0.1037 | 0.1889 | 0.2923 | 0.1520 | 0.3080 | 0.2426 | |
| 914 | 53.43° ± 4.80° | 89.87 ± 5.71m | 0.0409 | 0.0967 | 0.1738 | 0.3060 | 0.1347 | 0.3211 | 0.2813 | |
| 1882 | 59.58° ± 4.93° | 139.48 ± 39.55m | 0.0454 | 0.1044 | 0.1902 | 0.2891 | 0.1697 | 0.3195 | 0.2724 | |
| 41 | 60.90° ± 3.85° | 259.28 ± 8.43m | 0.0331 | 0.0644 | 0.1583 | 0.3698 | 0.1588 | 0.3726 | 0.2792 | |
| Pixel Size (Mean ± Stdev) | RTLSR Model Uncertainty | | | RTLSR Model: NBAR | | | RTLSR Model: NBAR Vegetation Indexes | | | |
| | Band3 | Band4 | Band5 | Band3 | Band4 | Band5 | NBAR-NDVI | NBAR-EVI | NBAR-NDVI | NBAR-EVI |
| 7.09 ± 4.39m | 0.0081 | 0.0128 | 0.0177 | 0.0389 | 0.1031 | 0.1937 | 0.3052 | 0.1489 | 0.3052 | 0.1489 |
| 31.53 ± 6.16m | 0.0010 | 0.0044 | 0.0059 | 0.0380 | 0.0816 | 0.1573 | 0.3168 | 0.1389 | 0.3168 | 0.1389 |
| 50.38 ± 5.56m | 0.0044 | 0.0078 | 0.0110 | 0.0423 | 0.1053 | 0.1904 | 0.2880 | 0.1414 | 0.2880 | 0.1414 |
| 67.81 ± 5.47m | 0.0015 | 0.0067 | 0.0105 | 0.0490 | 0.1105 | 0.2008 | 0.2898 | 0.1507 | 0.2898 | 0.1507 |
| 89.87 ± 5.71m | 0.0012 | 0.0061 | 0.0088 | 0.0437 | 0.0951 | 0.1763 | 0.2994 | 0.1432 | 0.2994 | 0.1432 |
| 139.48 ± 39.55m | 0.0024 | 0.0072 | 0.0089 | 0.0429 | 0.0972 | 0.1813 | 0.3023 | 0.1459 | 0.3023 | 0.1459 |
| 259.28 ± 8.43m | 0.0008 | 0.0012 | 0.0033 | 0.0315 | 0.0629 | 0.1250 | 0.3302 | 0.1225 | 0.3302 | 0.1225 |
| Accuracy Assessment | | | | Band3 | Band4 | Band5 | NBAR-NDVI | NBAR-EVI | NBAR-NDVI | NBAR-EVI |
| Measurement uncertainty without BRDF correction (Abs. / Rel.) | | | | 0.0110 / 21.09% | 0.0273 / 22.88% | 0.0397 / 18.16% | 0.0284 / 9.56% | 0.0120 / 7.38% | 0.0320 / 10.75% | 0.0671 / 36.27% |
| Measurement uncertainty with BRDF correction (Abs. / Rel.) | | | | 0.0051 / 12.50% | 0.0174 / 17.00% | 0.0284 / 14.97% | 0.0142 / 4.73% | 0.0099 / 6.76% | 0.0142 / 4.73% | 0.0099 / 6.76% |

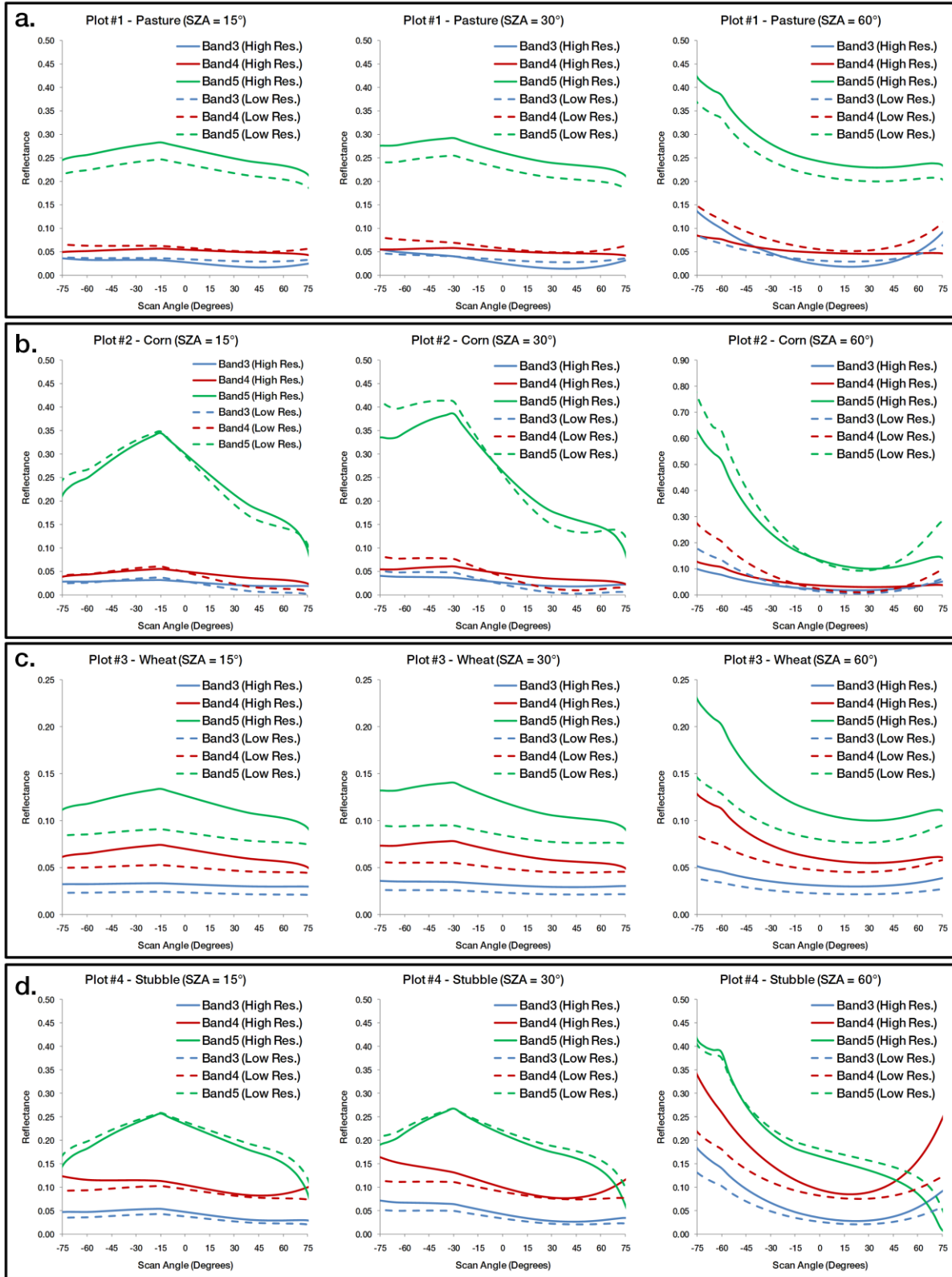


Fig. 9. Angular distribution of the BRDF in the principal plane (i.e., the vertical plane containing the Sun) for measurements taken over (a.) pasture; (b.) corn; (c.) senescent winter-wheat; and (d.) stubble land to examine the response of CAR bands #3 (0.472 μm), #4 (0.682 μm), and #5 (0.870 μm) at both moderate (low) and high spatial resolutions under different illumination conditions.

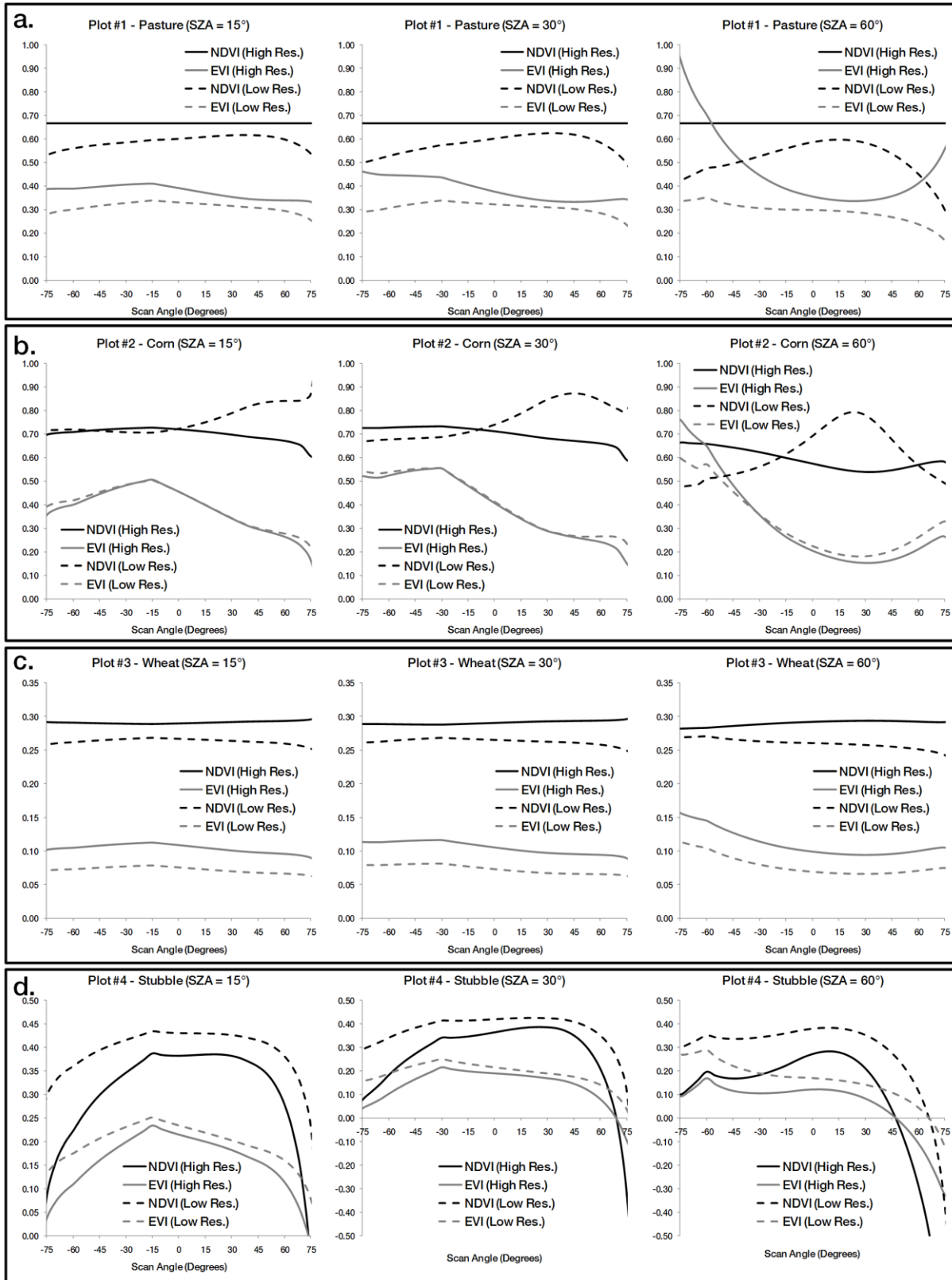


Fig. 10. Angular distribution of the BRDF in the principal plane for measurements taken over (a.) pasture; (b.) corn; (c.) senescent winter-wheat; and (d.) stubble land to examine the response of CAR-derived NDVI and EVI products at both moderate (low) and high spatial resolutions under different illumination conditions.

Plot #1 - Pasture

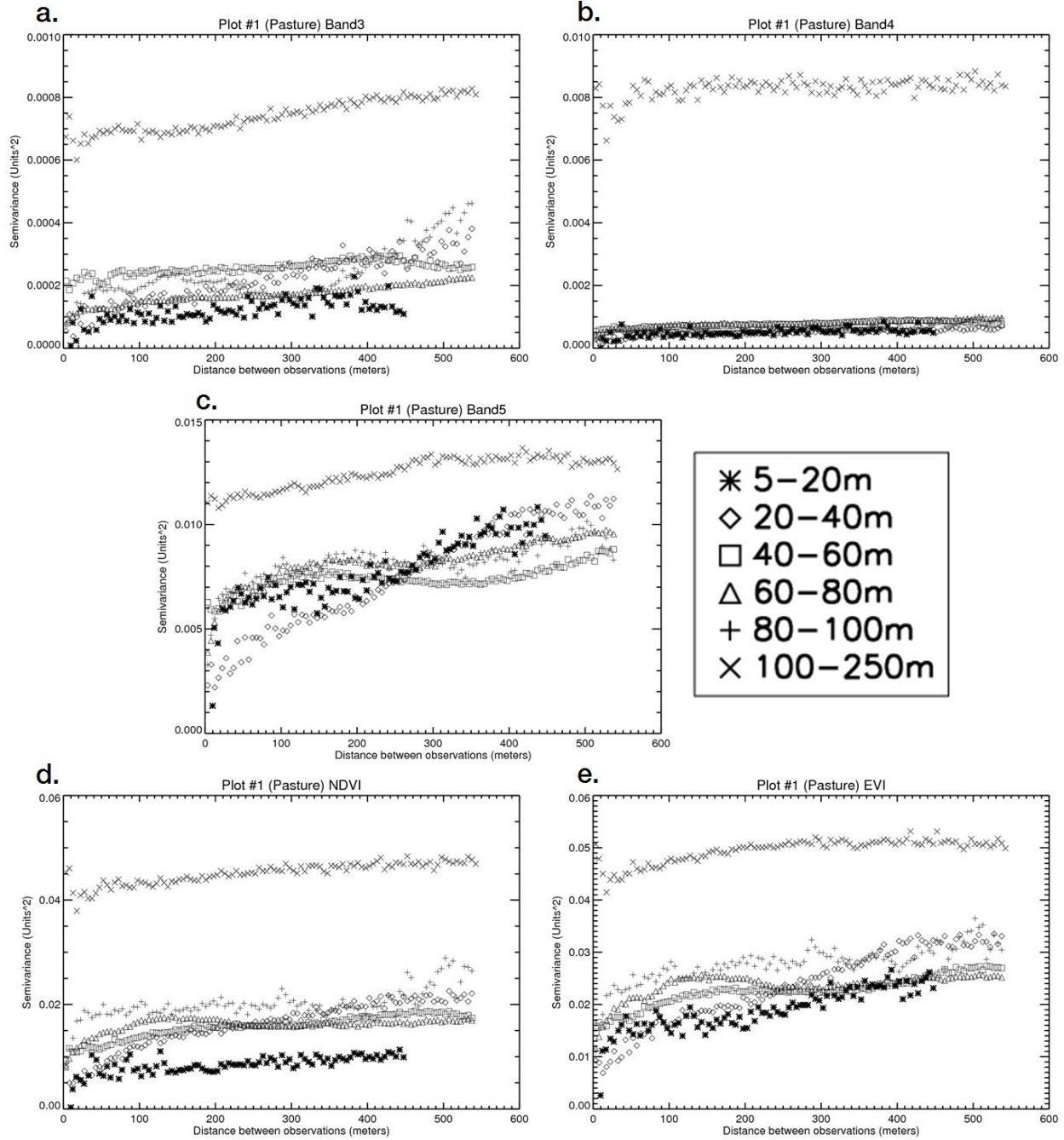


Fig. 11. Experimental variograms (Plot #1 – Pasture) show the variation in CAR retrievals as a function of spatial intervals and separation distance. Variograms include surface directional reflectances for (a.) CAR band #3 (0.472 μm), (b.) band #4 (0.682 μm), and (c.) band #5 (0.870 μm); as well as (d.) NDVI, and (e.) EVI.

Plot #2 - Corn

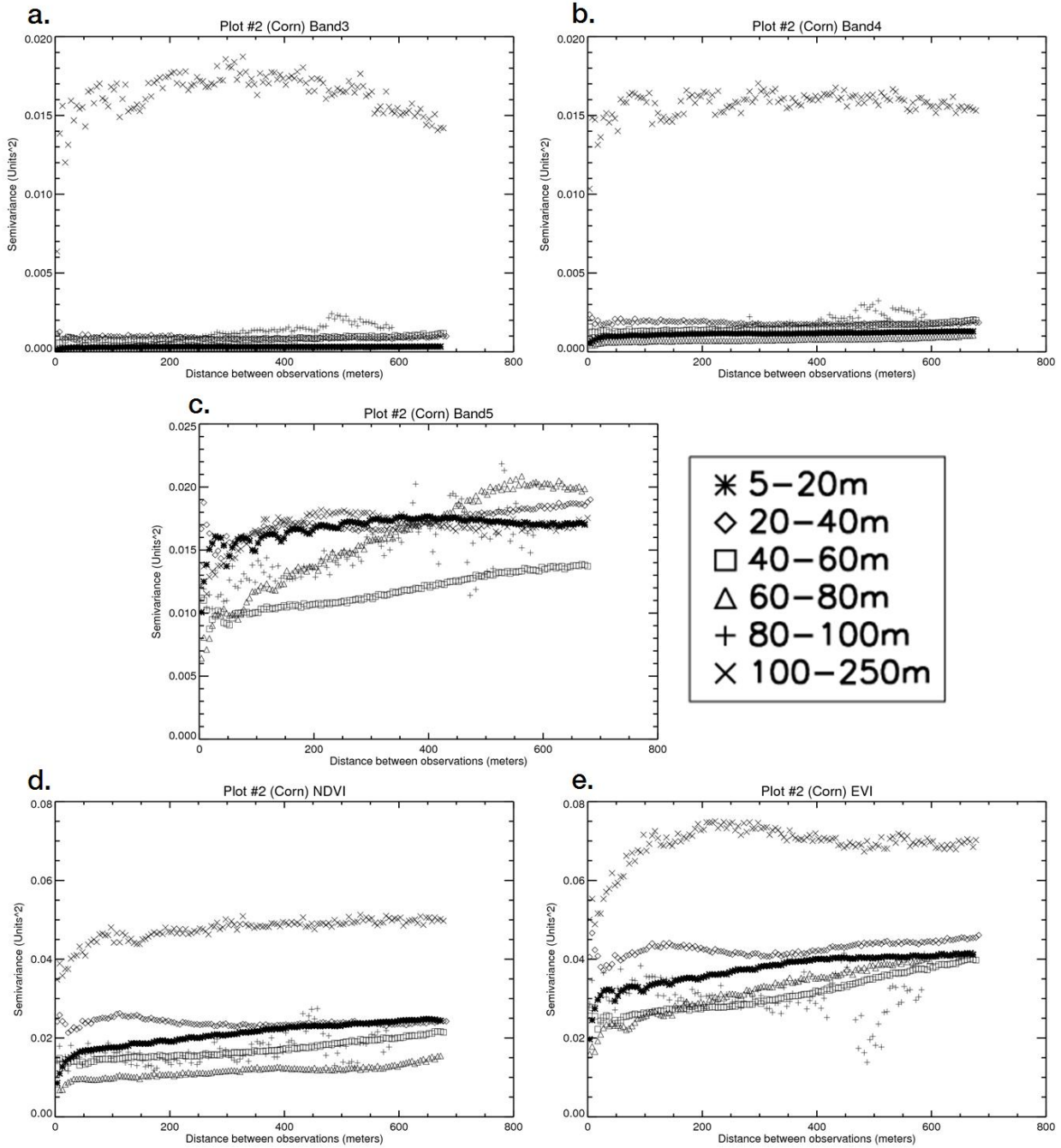


Fig. 12. Experimental variograms (Plot #2 – Corn) show the variation in CAR retrievals as a function of spatial intervals and separation distance. Variograms include surface directional reflectances for (a.) CAR band #3 (0.472 μm), (b.) band #4 (0.682 μm), and (c.) band #5 (0.870 μm); as well as (d.) NDVI, and (e.) EVI.

Plot #3 - Wheat

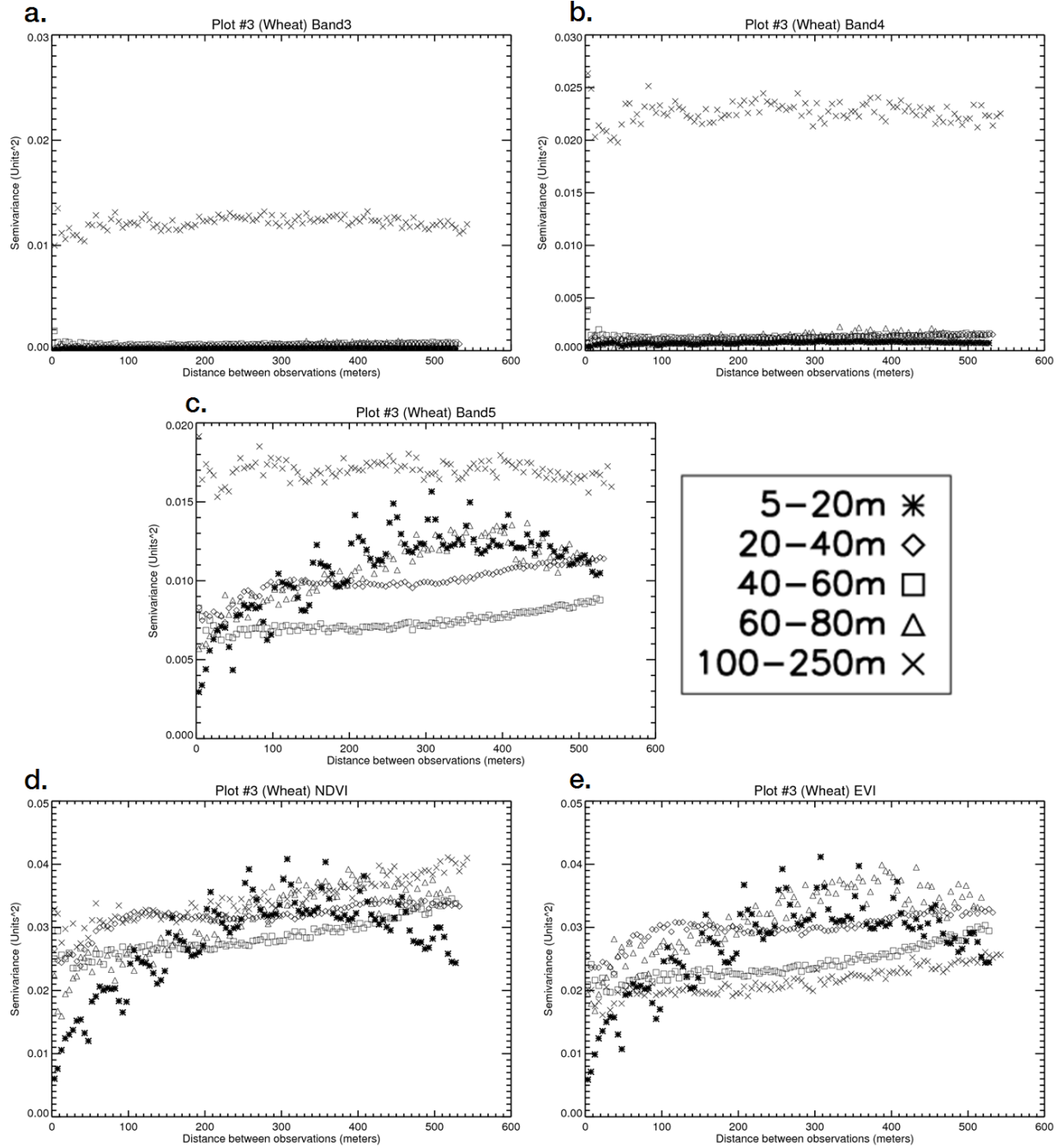


Fig. 13. Experimental variograms (Plot #3 – Wheat) show the variation in CAR retrievals as a function of spatial intervals and separation distance. Variograms include surface directional reflectances for (a.) CAR band #3 (0.472 μm), (b.) band #4 (0.682 μm), and (c.) band #5 (0.870 μm); as well as (d.) NDVI, and (e.) EVI.

Plot #4 - Stubble

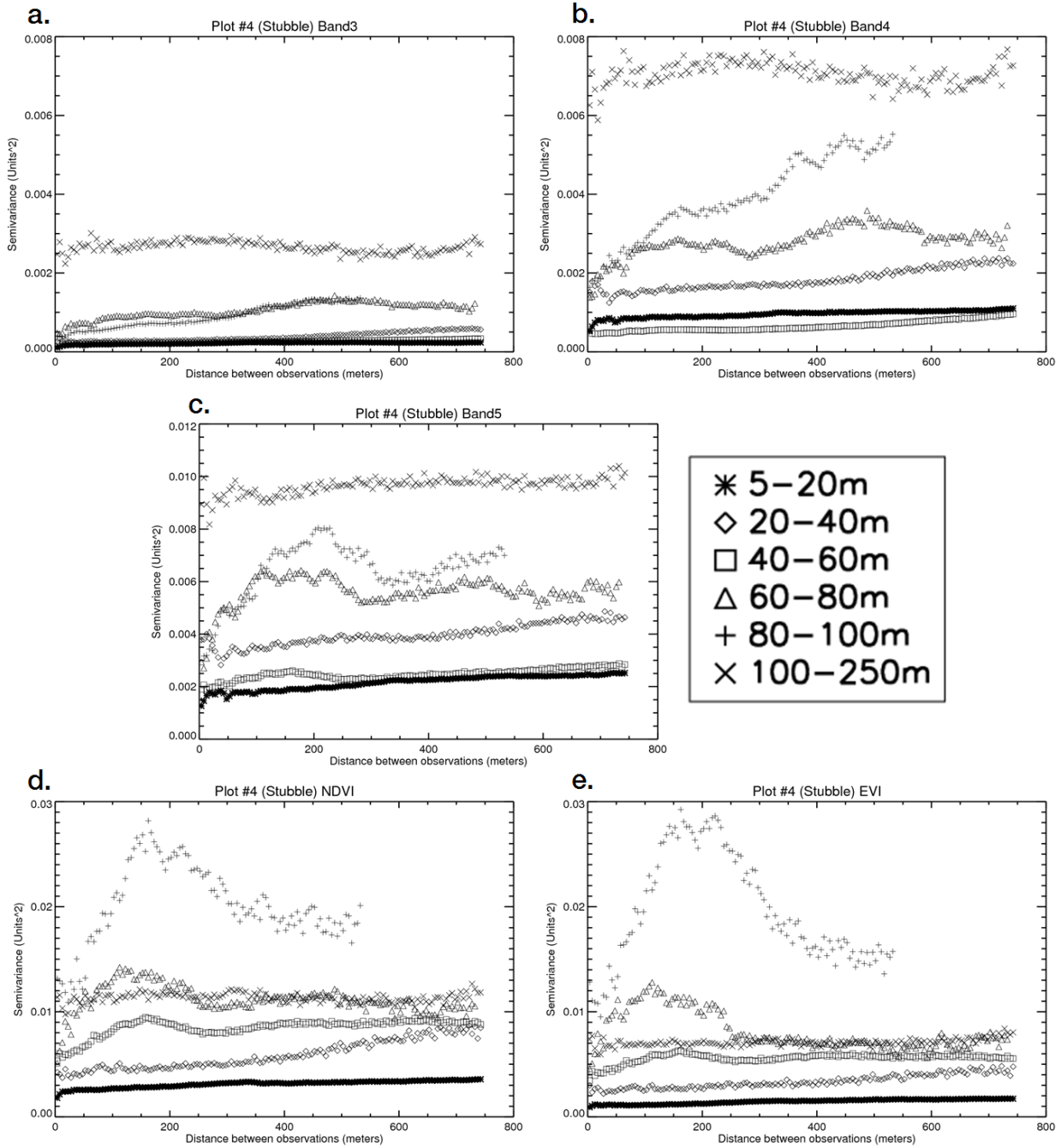


Fig. 14. Experimental variograms (Plot #4 – Stubble) show the variation in CAR retrievals as a function of spatial intervals and separation distance. Variograms include surface directional reflectances for (a.) CAR band #3 (0.472 μm), (b.) band #4 (0.682 μm), and (c.) band #5 (0.870 μm); as well as (d.) NDVI, and (e.) EVI.

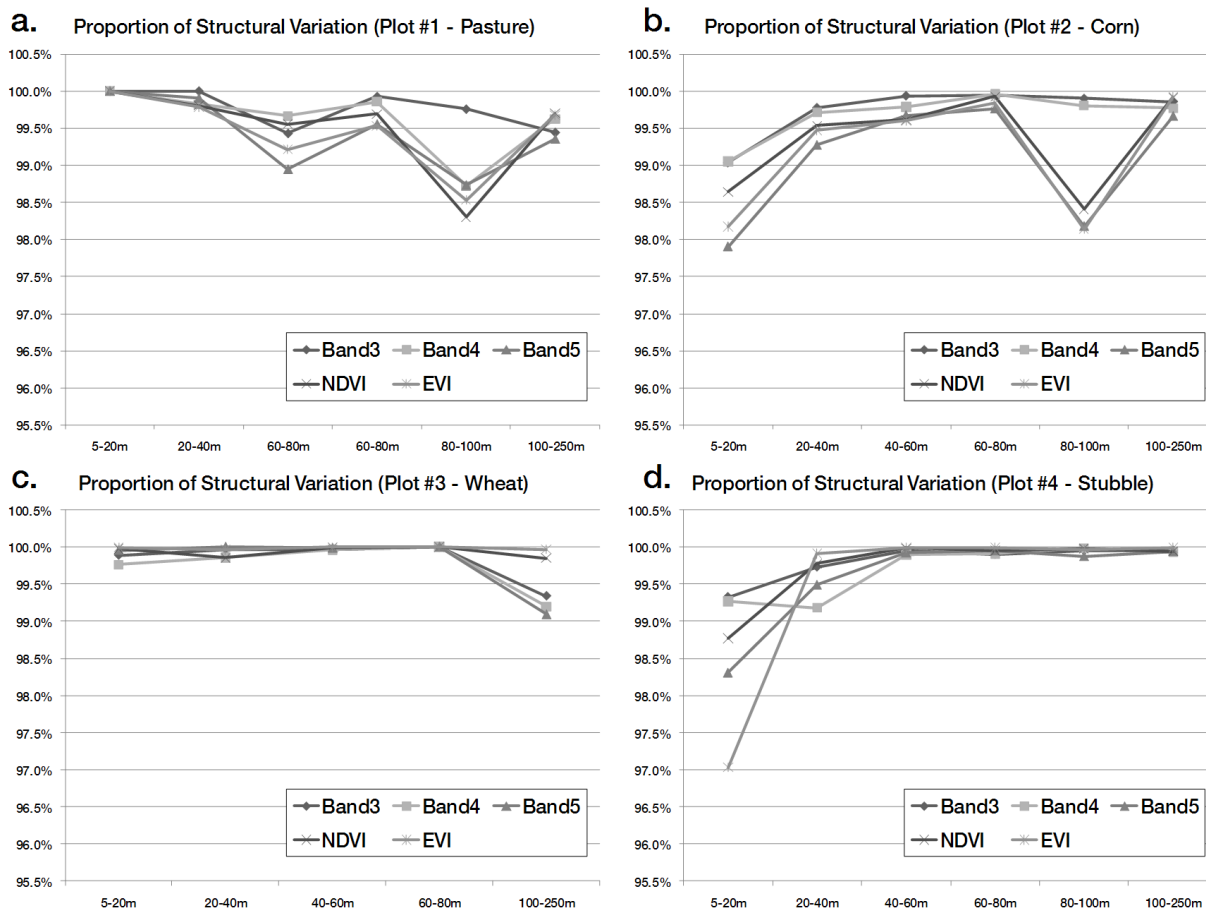


Fig. 15. The proportion of structural variation is shown as a function of spatial intervals for CAR band #3, #4, #5, NDVI, and EVI over (a.) pasture; (b.) corn; (c.) senescent winter-wheat; and (d.) stubble.